

1 **Solar radiation estimation in West Africa: impact of dust conditions during**  
2 **2021 dry season**

3

4 Léo Clauzel<sup>1</sup>, Sandrine Anquetin<sup>1</sup>, Christophe Lavaysse<sup>1</sup>, Gilles Bergametti<sup>2</sup>, Christel  
5 Bouet<sup>2,3</sup>, Guillaume Siour<sup>4</sup>, Rémy Lapere<sup>1</sup>, Béatrice Marticorena<sup>4</sup>, Jennie Thomas<sup>1</sup>

6

7 <sup>1</sup>Université Grenoble Alpes, IRD, CNRS, Grenoble-INP, IGE, 38000 Grenoble, France

8 <sup>2</sup>LISA, Université Paris Cité and Univ Paris Est Créteil, CNRS, F-75013 Paris, France

9 <sup>3</sup>Institut d'Ecologie et des Sciences de l'Environnement de Paris, UMR IRD 242, Univ Paris  
10 Est Créteil–Sorbonne Université–CNRS–INRAE–Université Paris Cité, F-93143 Bondy,  
11 France

12 <sup>4</sup>LISA, Univ Paris Est Créteil, Université Paris Cité, CNRS, LISA, F-94010 Créteil, France

13

14 *Correspondence to:* Léo Clauzel (leo.clauzel@univ-grenoble-alpes.fr)

## 15 **Abstract**

16 The anticipated increase in solar energy production in West Africa requires high-quality solar  
17 irradiance estimates, which is affected by meteorological conditions and in particular the  
18 presence of desert dust aerosols. This study examines the impact of incorporating desert  
19 dust into solar irradiance and surface temperature estimations. The research focuses on a  
20 case study of a dust event in March 2021, which is characteristic of the dry season in West  
21 Africa. Significant desert aerosol emissions at the Bodélé depression are associated with a  
22 Harmattan flow that transports the plume westwards. Simulations of this dust event were  
23 conducted using the WRF meteorological model alone, as well as coupled with the  
24 CHIMERE chemistry-transport model, using three different datasets for the dust aerosol  
25 initial and boundary conditions (CAM5, GOCART, MERRA2). Results show that considering  
26 desert dust reduces estimation errors in global horizontal irradiance (GHI) by about 75%.  
27 The dust plume caused an average 18% reduction in surface solar irradiance during the  
28 event. Additionally, the simulations indicated a positive bias in aerosol optical depth (AOD)  
29 and PM10 surface concentrations. The choice of dataset for initial and boundary conditions  
30 minimally influenced GHI, surface temperature, and AOD estimates, whereas PM10  
31 concentrations and aerosol size distribution were significantly affected. This study  
32 underscores the importance of incorporating dust aerosols into solar forecasting for better  
33 accuracy.

34

## 35 **Short summary**

36 Solar energy production in West Africa is set to rise, needing accurate solar irradiance  
37 estimates, which is affected by desert dust. This work analyses a March 2021 dust event  
38 using a modelling strategy incorporating desert dust. Results show that considering desert  
39 dust cut errors in solar irradiance estimates by 75% and reduces surface solar radiation by  
40 18%. This highlights the importance of incorporating dust aerosols into solar forecasting for  
41 better accuracy.

42

## 43 **1. Introduction**

44 The West African region is facing significant development challenges due to global change.  
45 One of these challenges is related to access to electricity, particularly through the use of  
46 renewable energy. West African countries have committed to reduce their greenhouse gas  
47 emissions as part of the Paris Agreement (2015). Furthermore, assessments of solar  
48 resources in West Africa demonstrate the region's substantial potential, as shown by  
49 Diabaté et al. (2004), Plain et al. (2019) and Yushchenko et al. (2018). The International  
50 Energy Agency (IEA) projects that the installed capacity for photovoltaic (PV) power  
51 generation will increase by almost 20 times from 2020 to 2030 under its Sustainable Africa  
52 Scenario (IEA, 2022). PV energy is expected to experience significant growth due to its  
53 competitiveness and low-carbon nature. However, solar production is highly dependent on  
54 weather conditions (Dajuma et al., 2016).

55 The growth of solar energy in West Africa calls for the development of tailored tools to  
56 facilitate its integration into power grids and ensure optimal operational maintenance.  
57 Accurate production forecasts are required by solar power plant operators, spanning various  
58 timescales, ranging from a few hours to several days. This is essential for maximising  
59 production, reducing penalties linked to predicted deliverable energy, and optimising plant  
60 maintenance to minimise production losses. High-quality forecasts are also crucial for  
61 electricity grid operators to maintain supply-demand equilibrium and ensure system stability.  
62 Therefore, the variability of energy production significantly affects them. The key

63 meteorological variables that influence photovoltaic production are the Global Horizontal  
64 Irradiance (GHI) and the air temperature. These factors, which directly impact electricity  
65 production and cell efficiency, often reach high levels in this region as demonstrated by  
66 Dajuma et al. (2016) and Ziane et al. (2021). Their findings indicate that solar irradiance is  
67 the primary factor influencing PV production, as the generated current by the photoelectric  
68 effect is proportional to the irradiance. Furthermore, they demonstrate that, at the second  
69 order, the air temperature affects the efficiency of solar cells, as both parameters are  
70 inversely correlated.

71  
72 Clauzel et al. (2024) identified desert dust aerosol as a significant source of GHI forecast  
73 errors for the only two solar power plants in the Sahel region of Sococim (Senegal) and  
74 Zagtoui (Burkina Faso), particularly during the dry season. Dust aerosols are a key element  
75 in the West African climate and strongly influence solar farm production through their direct  
76 effect (aerosol-radiation interaction (ARI), Briant et al., 2017) and indirect effects (aerosol-  
77 cloud interaction (ACI), Tuccella et al., 2019) on radiation, and also through their deposition  
78 on solar panels (fouling effect, Diop et al., 2020, Aidara et al., 2023). As mentioned by Kok et  
79 al. (2021), the West African desert aerosol load is the highest in the world and occurs mainly  
80 during the dry season. In fact, North Africa, including the Sahara, is the world's largest  
81 contributor to desert dust emissions (Prospero et al., 2002), and 60% of this dust is  
82 transported to the West African region (D'Almeida, 1986; Kok et al., 2021). Most dust  
83 emissions are associated with synoptic-scale atmospheric dynamics such as the Harmattan  
84 flow during the dry season (Klose et al., 2010). Engelstaedter and Washington (2007)  
85 pointed out the importance of small-scale wind events associated with the large-scale flow,  
86 especially in the Bodele depression, which is a hotspot for dust emissions (Engelstaedter et  
87 al., 2006). Analysing satellite observations, Schepanski et al. (2009) show that 65% of the  
88 activation of the dust source area occurred in the early morning, demonstrating the important  
89 role of the breakdown of the nocturnal low-level jet. Washington and Todd (2005) confirmed  
90 the importance of the Bodele low-level jets during the dry season in initiating dust emissions  
91 that can be transported to the West African coast within a few days. Dust aerosol emissions  
92 are also highly linked to Mesoscale Convective Systems (MCS, Marsham et al., 2008 ;  
93 Bergametti et al., 2017) and to strong near-surface winds in the intertropical discontinuity  
94 zone during the rainy season (Bou Karam et al., 2009).

95  
96 Some studies intend to model dust events in West Africa such as Ochiegbu (2021) who  
97 implemented a back-trajectories model to understand the dust event reaching Nigeria. This  
98 work revealed that most of the aerosols coming to Nigeria between 2011 and 2014 were  
99 originating from the Bodele Depression. Menut (2023) focused on dust forecasting during the  
100 Cloud-Atmospheric Dynamics-Dust Interactions in West Africa (CADDIWA) campaign during  
101 summer 2021 (Flamant et al., 2024) using the CHIMERE regional chemistry-transport model  
102 (Menut et al., 2021). The model was coupled online with the Weather Research and  
103 Forecasting (WRF) meteorological model (Briant et al., 2017; Tuccella et al., 2019) to  
104 perform dust aerosol concentration forecasts. The results of this work provide confidence in  
105 the model coupling in the region as the dust forecast quality does not decrease with time  
106 over a few days. In addition, only a limited number of studies have been conducted on the  
107 prediction of GHI in the West African region. Sawadogo et al. (2024) conducted an  
108 evaluation of WRF-solar GHI forecast (Jimenez et al., 2016) in Ghana for the year 2021. In  
109 their work, a version of the model coupled offline with Copernicus Atmosphere Monitoring  
110 Service (CAMS) Aerosol Optical Depth (AOD) forecasts was considered to integrate

111 information on aerosol load. They showed that WRF-Solar outperforms in predicting GHI  
112 under clear sky conditions while its performance under high aerosol levels remains poor, that  
113 was mainly attributed to uncertainties in the input AOD during data assimilation within the  
114 model. Close to the region of interest, for the northern Morocco area, El Alani et al. (2020)  
115 compared the performance of global models (Global Forecast System, Integrated Forecast  
116 System, McClear) and demonstrated their proficiency in capturing GHI hourly temporal  
117 variability.

118

119 As far as our knowledge is concerned, no studies have been conducted to assess online  
120 coupled simulations between a meteorological model and an aerosol life cycle model  
121 representing the emissions, the transport and the deposition in West Africa to estimate solar  
122 irradiance. This is despite the significant presence of desert dust, characterised by high  
123 concentrations in the region. Additionally, scarce attention has been given to the significance  
124 of initial and boundary conditions for conducting the aerosol model on the performance of  
125 analysis simulations, and to our knowledge, investigating these aspects would represent a  
126 novel contribution to research in the West African region.

127

128 Within this general context, the objectives of this study are two folds i) to evaluate the ability  
129 to reproduce a dust event using a meteorological and dust life cycle model coupling  
130 configuration, and ii) to investigate whether the performance of the simulations can be  
131 enhanced by modifying the aerosol initial and boundary conditions employed, and to  
132 estimate the uncertainty associated with this dataset selection with regard to the errors made  
133 by the model. Section 2 introduces the case study, the simulation configuration, the data and  
134 models selected for this work. In Section 3, the results are presented, beginning with the  
135 variables of interest for solar production (GHI and surface air temperature), followed by the  
136 variables associated with the desert aerosols (AOD, concentration, size distribution,  
137 emissions). Section 4 gives main conclusions and draws some perspectives for this study.

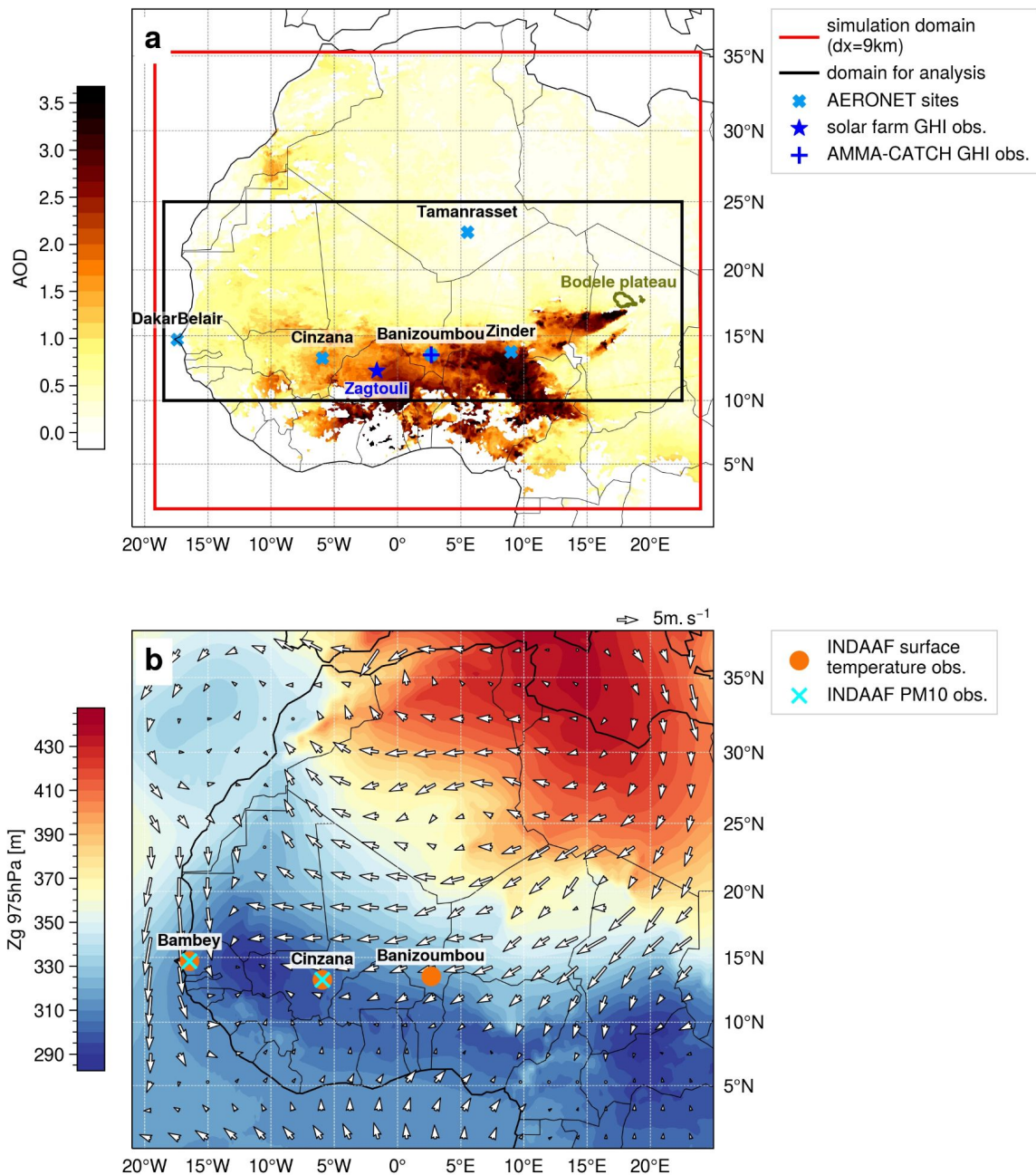
138

## 139 **2. Material and methods**

### 140 **2.1. Case study**

141 The case study is a dust event that occurs in West Africa from March 26<sup>th</sup>-00 UTC to April  
142 2<sup>nd</sup>-00 UTC, 2021, i.e., during the dry season. High dust emissions occur at the Bodélé  
143 Depression (Chad), the plume being then transported westward. The dust plume reached its  
144 maximum intensity in terms of AOD and dust concentration over West Africa, and in  
145 particular over the Zagtouli solar farm (Burkina-Faso, Fig. S1), on March 30<sup>th</sup>. The event  
146 was also chosen because it was not predicted in the solar forecast currently implemented for  
147 the Zagtouli solar farm, leading to solar forecast errors during the passage of the dust plume  
148 (Clauzel et al., 2024).

149 Figure 1 illustrates that this event is characterised by a strong Harmattan flow, with surface  
150 winds from the South/South-West sweeping across the Bodélé Depression (Chad), where  
151 the potential for desert dust emissions is very high (Prospero et al., 2002; Washington et al.,  
152 2006). Additionally, this event is characterised by a westward flow between Chad and the  
153 Atlantic coast, which facilitates the transportation of the dust plume. Fig. 1a shows  
154 MODerate-resolution Imaging Spectroradiometer (MODIS) satellite observations of the AOD,  
155 identifying the initial dust source area on the Bodélé Depression, as well as the westward  
156 movement of the plume. This event is characteristic of the West African dry season  
157 climatology, with a dominant Harmattan flow as described in the introduction. Figure S1  
158 provides further insight into the dust plume transport during the case study.



160  
 161 **Figure 1** - a) Mean aerosol Optical Depth at 550nm from MODIS satellite observations over  
 162 the period 28 March-00 UTC to 02 April-00 UTC 2021. The Global Horizontal Irradiance  
 163 (GHI) observations and AERONET aerosol measurement network, introduced in 2.4, are  
 164 presented, as well as the boundaries of the simulated domain (red rectangle) and the area of  
 165 interest for analysis (black rectangle). b) Mean synoptic conditions of the geopotential height  
 166 (Zg) at 975hPa and the 10m-wind (white arrows - in m/s) over the period 28 March-00 UTC  
 167 to 02 April-00 UTC 2021 from ERA5 reanalysis. The surface temperature and aerosol  
 168 concentration observations from the INDAAF network, introduced in 2.4, are presented.

169

170

171

## 2.2. Modelling tools

### 2.2.1. WRF model

172 The meteorological Weather and Research and Forecasting model (WRF) model version  
 173 3.7.1 is taken for compatibility with the CHIMERE coupling procedure. It is used in its non-  
 174 hydrostatic configuration (Skamarock et al., 2008) and is forced at the boundaries of the  
 175 domain every hour by the meteorological reanalysis data of ERA5 (ECMWF) provided on a  
 176 regular 0.25° x 0.25° grid.

177 The model is run with a 9 km horizontal resolution, a 45s integration time step and 50  
 178 vertical levels, from the surface to 50 hPa. The updated Rapid Radiative Transfer Model  
 179 (RRTMG) radiation scheme (Iacono et al., 2008), which is mandatory for the aerosol optical  
 180 properties feedback, is employed for both long- and short-wave radiations. Additionally, the  
 181 Thompson aerosol-aware microphysics scheme (Thompson and Eidhammer, 2014) is  
 182 applied. The Yonsei University planetary boundary layer's surface layer scheme (Hu et al.,  
 183 2013) is also used, and the cumulus parameterisation is based on the Grell-Freitas scheme  
 184 (Arakawa, 2004). The Revised MM5 surface layer scheme (Jiménez et al., 2012) is  
 185 employed, while the Noah-MP Land Surface Model (Niu et al. 2011) is implemented for the  
 186 land surface physics scheme.

187

188

### 2.2.2. CHIMERE model

189 The chemistry-transport model CHIMERE version v2020r3 (Menut et al., 2021) is used in  
 190 conjunction with the WRF model. Both models have a 9 km horizontal grid. The CHIMERE  
 191 model has 30 pressure-dependent vertical levels from the surface up to 200 hPa, with a first  
 192 layer thickness of 3 hPa. The model is configured for dust-only, with no chemistry and only  
 193 considering dust aerosols (details in section 2.3). The threshold friction velocities for dust  
 194 emission are estimated using the Shao and Lu scheme (2000) and the 6-km spatial  
 195 resolution GARLAP (Global Aeolian Roughness Lengths from ASCAT and PARASOL)  
 196 dataset from Prigent et al. (2012). Mineral dust emission fluxes were calculated employing  
 197 the Alfaro and Gomes (2001) scheme on 10 aerosol size bins ranging from 0.01 to 40 µm.  
 198 The Fécan et al. (1999) parametrization is employed to account for the inhibitory effect of  
 199 soil moisture on dust emission. Dry deposition is treated as described in Zhang et al. (2001).  
 200 Wet scavenging for aerosol is computed following the Willis and Tattelman scheme (1989).  
 201 The CHIMERE model includes the Fast-JX module, version 7.0b (Wild et al., 2000; Bian et  
 202 al., 2002) for the calculation of radiative processes. It considers the radiative properties for  
 203 each aerosol species and each aerosol size bin independently to compute the aerosol  
 204 optical depths, the single scattering albedo and the aerosol asymmetry factor. More details  
 205 on the dust aerosol radiative properties are given in Tables S1 and S2. Finally, we test three  
 206 different initial and boundary condition datasets for mineral dust load (see 2.2.3).

207

208 **Table 1** - Parameterizations used in WRF and CHIMERE

<b>WRF</b>	
microphysics	Thompson aerosol-aware (Thompson and Eidhammer, 2014)
radiation	RRTMG scheme for LW and SW (Iacono et al., 2008)
land surface	Noah-MP land surface scheme (Niu et al., 2011)
planetary boundary layer	Yonsei University scheme

	(Hu et al., 2013)
surface layer	Revised MM5 surface layer scheme (Jimenez et al., 2012)
cumulus	Grell-Freitas scheme (Arakawa, 2004)
<b>CHIMERE</b>	
threshold friction velocities	Shao and Lu (2000) scheme
soil moisture	Fécan et al. (1999) scheme
dust emission fluxes	Alfaro and Gomes (2001) scheme
radiative processes	Fast-JX model, version 7.0b (Wild et al., 2000; Bian et al., 2002)
aerosol size distribution bins (diameters in $\mu\text{m}$ )	0.010 - 0.022
	0.022 - 0.048
	0.048 - 0.107
	0.107 - 0.235
	0.235 - 0.516
	0.516 - 1.136
	1.136 - 2.500
	2.500 - 5.000
	5.000 - 10.00
10.00 - 40.00	

209

210

### 2.2.3. Dust aerosol initial and boundary condition datasets

211 In this study, the uncertainty in the solar estimate associated with the initial and boundary  
 212 conditions of the dust aerosol load is evaluated. Three datasets were used: a climatology  
 213 derived from the Global Ozone Chemistry Aerosol Radiation and Transport (GOCART,  
 214 Ginoux et al., 2001), the Modern-Era Retrospective analysis for Research and Applications  
 215 Version 2 (MERRA2) reanalysis (Gelaro et al., 2017) and the CAMS reanalysis (Inness et  
 216 al., 2019).

217 The GOCART climatology is provided with the distribution of the CHIMERE model. It is a  
 218 monthly climatology on a coarse horizontal grid ( $2^\circ \times 2.5^\circ$ ), which is corrected by applying a  
 219 factor of 0.3 as in Vautard et al. (2005).

220 The MERRA2 reanalysis combines the Goddard Earth Observing System (GEOS) and  
 221 GOCART models, which are online coupled and implemented with a data assimilation  
 222 system. It has a 3-hour temporal resolution and is presented on a  $0.5^\circ \times 0.635^\circ$  horizontal  
 223 grid. The observational data considered in the data assimilation process are AOD satellite  
 224 observations from MODIS, Advanced Very High Resolution Spectroradiometer (AVHRR),  
 225 Multi-angle Imaging SpectroRadiometer (MISR) and ground observations from the AEROSOL  
 226 RObotic NETwork (AERONET).

227 The CAMS reanalysis was constructed using 4DVar data assimilation in ECMWF's  
 228 Integrated Forecast System (IFS). It has a temporal resolution of 3 hours and is computed  
 229 on a regular  $0.75^\circ$  horizontal grid. The AOD data from the Visible Infrared Imaging

230 Radiometer Suite (VIIRS), the MODIS and the Infrared Atmospheric Sounding Interferometer  
 231 (IASI) satellite observations are used as observational information in the data assimilation  
 232 process. The version 48R1 of CAMS is used in this study.

233 These three dust aerosol initial and boundary datasets differ in type (climatological or  
 234 reanalysis), in horizontal, vertical and temporal resolution, and in the resolution and range of  
 235 their aerosol size distribution. While GOCART has the highest number of aerosol classes  
 236 with 7 bins, CAMS covers a wider size spectrum despite a lower size resolution with only 3  
 237 classes. MERRA2 has an intermediate resolution with 5 classes, but covers a smaller  
 238 particle size spectrum than CAMS. The CHIMERE model pre-processes these dust aerosol  
 239 size distributions by applying a transfer coefficient  $\delta$  to compute the dust aerosol  
 240 concentration on the 10 aerosol size bin defined for the simulations :

$$c_j = \sum_i \delta_{i,j} \times c_i \quad (1)$$

241 where  $c_i$  is the dust aerosol concentration of the  $i^{th}$  size bin from the initial and boundary  
 242 condition dataset considered,  $c_j$  is the dust aerosol concentration of the  $j^{th}$  size bin in the  
 243 CHIMERE simulation, and  $\delta_{i,j}$  is the transfer coefficient. This transfer coefficient is derived  
 244 as :

- 245 -  $\delta_{i,j}=0$  if the  $i^{th}$  size bin from the initial and boundary condition dataset is found to be  
 246 wholly outside the  $j^{th}$  size bin in the CHIMERE simulation;
- 247 -  $\delta_{i,j}=1$  if the  $i^{th}$  size bin from the initial and boundary condition dataset is wholly  
 248 encompassed by the  $j^{th}$  size bin in the CHIMERE simulation;
- 249 -  $\delta_{i,j} = \frac{\log(r_{j,max}) - \log(r_{j,min})}{\log(R_{i,max}) - \log(R_{i,min})}$  if the  $i^{th}$  size bin from the initial and boundary condition  
 250 dataset wholly encompasses the  $j^{th}$  size bin in the CHIMERE simulation;
- 251 -  $\delta_{i,j} = \frac{\log(R_{i,max}) - \log(r_{j,min})}{\log(R_{i,max}) - \log(R_{i,min})}$  if the  $i^{th}$  size bin from the initial and boundary condition  
 252 dataset partially overlaps the  $j^{th}$  size bin in the CHIMERE simulation, but extends  
 253 below the start of this size bin;
- 254 -  $\delta_{i,j} = \frac{\log(r_{j,max}) - \log(R_{i,min})}{\log(R_{i,max}) - \log(R_{i,min})}$  if the  $i^{th}$  size bin from the initial and boundary condition  
 255 dataset partially overlaps the  $j^{th}$  size bin in the CHIMERE simulation, but extends  
 256 beyond the end of this size bin;

257 where  $R_{i,min}$  and  $R_{i,max}$  are respectively the radius of the lower and upper limit of the  $i^{th}$  size  
 258 bin from the initial and boundary condition dataset, and  $r_{j,min}$  and  $r_{j,max}$  are respectively the  
 259 radius of the lower and upper limit of the  $j^{th}$  size bin in the CHIMERE simulation.

260  
 261 For the sake of simplicity, throughout this article, we will refer to the WRF-CHIMERE  
 262 simulations runned with the GOCART, the MERRA2, and the CAMS dust aerosol initial and  
 263 boundary conditions as *wrf\_chimere-G*, *wrf\_chimere-M*, and *wrf\_chimere-C* simulations  
 264 respectively.

265 Table 2 summarises the characteristics of the three dust aerosol datasets and their  
 266 associated size distributions.

267



268 **Table 2.** Summary of the characteristics of the dust initial and boundary condition products.

	<b>GOCART</b>	<b>MERRA2</b>	<b>CAMS</b>
type	climatology	reanalysis	reanalysis
temporal resolution	monthly	3h	3h
vertical levels	20	72	60
horizontal resolution (lat x lon)	2°x2.5°	0.5°x0.635°	0.75°x0.75°
dust aerosol size distribution (radius in $\mu\text{m}$ )	0.20 - 0.36 $\mu\text{m}$	0.1 - 1.0 $\mu\text{m}$	0.03 - 0.55 $\mu\text{m}$
	0.36 - 0.60 $\mu\text{m}$	1.0 - 1.8 $\mu\text{m}$	0.55 - 0.90 $\mu\text{m}$
	0.60 - 1.20 $\mu\text{m}$	1.8 - 3.0 $\mu\text{m}$	0.90 - 20.00 $\mu\text{m}$
	1.20 - 2.00 $\mu\text{m}$	3.0 - 6.0 $\mu\text{m}$	
	2.00 - 3.60 $\mu\text{m}$	6.0 - 10.0 $\mu\text{m}$	
	3.60 - 6.00 $\mu\text{m}$		
	6.00 - 12.00 $\mu\text{m}$		

269

270

### 2.3. Modelling strategy

271 The domain of simulation extends from 2° to 35°N and from 19°W to 24°E, as illustrated by  
 272 the red box in Figure 1b. The domain is large enough to represent the primary atmospheric  
 273 flows, including the Harmattan North/North-West flow and the monsoon South flow, as well  
 274 as the transport of the emitted aerosol plumes. A horizontal resolution of 9 km has been  
 275 selected in order to ensure that the grid ratio is approximately 3 with the ERA5  
 276 meteorological forcing. This choice is also motivated by the a priori intention to achieve a  
 277 resolution higher than that of previous CHIMERE simulations performed in this region and  
 278 compared to the operational solar forecast model used for the Zagtouli solar farm, which are  
 279 based on global forecast models (see 2.4.1). The CHIMERE model is configured in a “dust  
 280 only” model, which models only the mineral dust type. This hypothesis is supported for this  
 281 dust case study by Fig. S2, as desert dust is the dominant aerosol during the event,  
 282 particularly above 10°N. This hypothesis is also reinforced by the dust optical depth (DOD)  
 283 to AOD ratio derived from the CAMS reanalysis, which exceeds 80% during this case study  
 284 and for the domain of interest (not shown). It is notable that biomass burning, which  
 285 represents the other principal aerosol source in this region, is no longer a significant  
 286 contributor to aerosol levels at that time of the year (Evans et al., 2018).

287 The WRF and CHIMERE models are coupled online through the OASIS3 MCT coupler. A  
 288 two-way coupling strategy is selected, in which WRF sends meteorological variables to  
 289 CHIMERE which in turn exchanges aerosol information such as AOD, Single Scattering  
 290 Albedo (SSA) and Asymmetry Factor. This coupling strategy imposes most of the WRF  
 291 parameterisations. The exchange frequency is set to 15 minutes. The WRF model computes  
 292 fields on 50 levels, which are linearly interpolated over the 30 CHIMERE vertical levels via  
 293 the OASIS coupler. The coupling includes the feedbacks of aerosol-radiation interactions

294 (ARI, direct aerosol effect) and aerosol-cloud interactions (ACI, indirect aerosol effects)  
295 simultaneously.

296 The simulation starts on March 14th-00 UTC and ends on April 2nd-00 UTC, 2021. The first  
297 two weeks served as the spin-up period. The simulation outputs are analysed for the period  
298 of March 28th-00 UTC to April 2nd-00 UTC, which corresponds to the passage of the  
299 dust plume in the Sahel region, in particular around the Zagtouli solar farm in Burkina Faso.  
300 Four simulations were conducted: a meteorological simulation using WRF model alone, and  
301 dust simulations with the coupled WRF-CHIMERE models using as initial and boundary  
302 conditions the GOCART climatology, the MERRA2 reanalysis and the CAMS reanalysis. The  
303 simulation using only WRF allows for the evaluation of the impact of taking into account dust  
304 aerosols in estimating solar irradiance. This is compared to the other three simulations,  
305 which are also used to evaluate the uncertainties associated with the choice of the aerosol  
306 initial and boundary condition dataset. A domain of interest, spanning 10°N to 25°N (Fig. 1a),  
307 was selected for analysis and comparisons. This choice was guided by the dust plume  
308 trajectory (Fig. S1) and the “dust only” hypothesis (Fig. S2).

309

## 310 **2.4. Evaluation datasets**

311 This section presents the local and regional data that are employed in the evaluation of the  
312 simulations.

### 313 **2.4.1. GHI**

314 The Global Horizontal Irradiance (GHI) is the total shortwave irradiance from the Sun on a  
315 horizontal surface on Earth. It is the sum of direct irradiance, which takes into account the  
316 solar zenith angle, and diffuse horizontal irradiance. It is measured in  $W.m^{-2}$  for the  
317 wavelength range 0.3 - 3.0  $\mu m$ .

318

319 The national electricity company of Burkina-Faso, Sonabel, operates a solar farm in Zagtouli  
320 (12.31°N;1.64°W; Fig. 1a), approximately 15 km west of the capital, Ouagadougou. It has an  
321 installed capacity of 34 MWp and contributes up to 4% of Burkina Faso's annual electricity  
322 production. Ground GHI measurements from pyranometers are available at a temporal  
323 resolution of 15 minutes for the Zagtouli solar plant and undergo pre-processing to ensure  
324 quality control. This involves removing outliers and days with missing data, visually checking  
325 the consistency of the measured values and selecting data corresponding to production  
326 hours (positive values for solar irradiance at the top of the atmosphere). Operational GHI  
327 forecasts for this solar farm are computed by the French company Steadysun. These  
328 forecasts are based on a multi-model, multi-member and multi-mesh grid aggregation, which  
329 is derived from the NCEP Global Ensemble Forecast System and the ECMWF Integrated  
330 Forecast System (Clauzel et al., 2024).

331 In-situ measurements of GHI from pyranometers (Fig. 1a) are also available at a 15-minutes  
332 temporal resolution for the Banizoumbou (Niger) surface station, installed as part of the  
333 AMMA-CATCH observatory (Analyse Multidisciplinaire de la Mousson Africaine - Couplage  
334 de l'Atmosphère Tropicale et du Cycle Hydrologique, AMMA-CATCH (2005)).

335 The two measurement sites were selected because they are the only locations where GHI  
336 observations have been made available along the dust plume transport for the case study,  
337 with the Zagtouli power station being one of the first large solar farms in West Africa and the  
338 AMMA-CATCH observatory being the only one to offer continuous GHI measurements for  
339 the region and period of interest.

340

341 The CAMS gridded solar radiation dataset (CAMS solar radiation services v4.6, Schroedter-  
 342 Homscheidt et al., 2022), based on the Heliosat-4 method (Qu et al., 2017), provides several  
 343 variables related to solar irradiance, such as clear-sky and all-sky GHI. It has a horizontal  
 344 resolution of 0.1°x0.1° and provides data every 15 minutes. The clear sky model includes  
 345 aerosols through the CAMS chemical transport model (Inness et al., 2019), which integrates  
 346 data assimilation of AOD and is coupled online to a numerical weather prediction model.  
 347 Cloud information for the all-sky model is derived from MeteoSat Second Generation (MSG)  
 348 satellite observations using the AVHRR Processing scheme Over cLOUDs, Land and Ocean  
 349 (APOLLO) Next Generation cloud processing scheme (Klüser et al., 2015). The dataset was  
 350 selected for comparison with the simulations as it integrates a description of aerosol  
 351 processes. While Yang and Bright (2020) and Sawadogo et al. (2023) show that it is the best  
 352 performing product for estimating surface solar irradiance in the West African region among  
 353 several satellite-based gridded irradiance products, this dataset still has a negative bias of  
 354 about 10% for all-sky solar irradiance estimates at desert stations in North Africa (CAMS  
 355 solar radiation regular validation report, Lefèvre, 2022).

356

357

#### 2.4.2. Surface temperature

358 In-situ surface temperature measurements are available for three stations of the  
 359 International Network to study Deposition and Atmospheric composition in Africa (INDAAF) :  
 360 Banizoumbou (Niger, 13.54° N, 2.66° E, 6.2m above surface; Rajot et al, 2010a; Marticorena  
 361 et al, 2010; Kaly et al., 2015), Cinzana (Mali, 13.28° N, 5.93° W, 2m above surface; Rajot et  
 362 al, 2010b; Marticorena et al, 2010; Kaly et al., 2015) and Bambey (Senegal, 14.70° N,  
 363 16.47° W, 5.2m above surface; Marticorena et al, 2021a) (Fig. 1b). The measurement sites  
 364 were selected since they are almost aligned around 13-15° North, which represents the main  
 365 pathway of Saharan and Sahelian dust towards the Atlantic Ocean during the case study.  
 366 The ERA5 atmospheric reanalysis (Hersbach et al., 2020) provides spatially continuous  
 367 hourly values of surface temperature at 2 metres and has a horizontal resolution of 0.25° x  
 368 0.25°.

369

370

#### 2.4.3. Aerosol

371 The INDAAF network also provides data on aerosol concentration through ground  
 372 measurements of PM<sub>10</sub>, i.e. the concentration of atmospheric particles having an  
 373 aerodynamic diameter less than 10 µm. For this case study, hourly PM<sub>10</sub> measurements are  
 374 available for two stations (Fig. 1b): Cinzana (Rajot et al, 2010c; Marticorena et al, 2021; Kaly  
 375 et al, 2015) and Bambey (Marticorena et al, 2021b).

376 The CAMS atmospheric reanalysis (Inness et al., 2019) is also used to evaluate regional  
 377 surface PM<sub>10</sub> concentration and AOD. It provides 3-hourly data with a horizontal resolution of  
 378 0.75° x 0.75°, with a surface layer thickness of 2.4 hPa.

379

380 Local ground measurements of AOD are retrieved from the AErosol RObotic NETwork level  
 381 1.5 dataset (AERONET, Holben et al., 1998; Giles et al., 2019). AOD is calculated from sun  
 382 photometer recordings, along with Ångström Exponent, and is only available during clear sky  
 383 conditions in daylight hours, with a resolution of 1 minute. The AOD at 400 nm simulated  
 384 with the WRF-CHIMERE model is converted to 440 nm for comparison with AERONET,  
 385 using the Ångström formula :

$$\frac{AOD_{\lambda}}{AOD_{\lambda_0}} = \left( \frac{\lambda}{\lambda_0} \right)^{-\alpha} \quad (2)$$

386 where  $AOD_{\lambda}$  is the AOD at the desired wavelength,  $\lambda=440\text{ nm}$  here ;  $AOD_{\lambda_0}$  is the AOD at  
 387 the wavelength simulated in the model,  $\lambda_0=400\text{ nm}$  here ;  $\alpha$  is the Ångström exponent,  
 388 derived from the simulated AOD at different wavelengths and here given for the range from  
 389 400 nm to 600 nm.

390  
 391 AERONET also provides an aerosol size distribution dataset estimated through inversion of  
 392 the photometers data, as described in Dubovik and King (2000). The algorithm for inversion  
 393 provides a volume particle size distribution for 22 bins, which are logarithmically distributed  
 394 for radii between 0.05  $\mu\text{m}$  and 15  $\mu\text{m}$ . For comparison with the modelled aerosol size  
 395 distribution, this distribution is interpolated on the CHIMERE simulated aerosol size  
 396 distribution which is composed of 10 bins ranging from 0.01  $\mu\text{m}$  to 40.00  $\mu\text{m}$  in diameter (see  
 397 Table 1). Given that the coarsest bin (10.00-40.00  $\mu\text{m}$ ) is at the limit of the capabilities of the  
 398 inversion method, and the two thinnest bins (0.010-0.022  $\mu\text{m}$  and 0.022-0.048  $\mu\text{m}$ ) are out of  
 399 the range of the inversion product, the AERONET dataset size sections are interpolated on  
 400 the CHIMERE size sections ranging from 0.048 to 10.0  $\mu\text{m}$ . Consequently, only comparisons  
 401 between the three simulations can be made for the three size sections which are out of the  
 402 range of AERONET product. The column aerosol volume size distribution simulated by the  
 403 model is calculated for each bin “i” as in Menut et al. (2016) :

$$\frac{dV(r_i)}{d \ln(r_i)} = \sum_{k=1}^{nlevels} \frac{m_{k,r_i} \times \Delta z_k}{\rho_{dust} \times \ln(r_{i,max}/r_{i,min})} \quad (3)$$

404 where  $r_i$  is the mean mass median radius (in  $\mu\text{m}$ ) and  $r_{i,min}$  and  $r_{i,max}$  the boundaries of the  
 405  $i^{th}$  bin.  $m_{k,r_i}$  is the dust aerosol mass concentration (the mass of aerosol in one cubic metre  
 406 of air, in  $\mu\text{g} \cdot \text{m}^{-3}$ ).  $\rho_{dust}$  is the dust aerosol density (the mass of the particle in its own volume,  
 407  $\rho_{dust}=2300\text{ kg} \cdot \text{m}^{-3}$ ).  $\Delta z_k$  is the model layer thickness (in metres), for a total of n levels (here  
 408 30 vertical levels).

409  
 410 The locations of the five AERONET sites used for comparison in this study are illustrated in  
 411 Figure 1a.

412  
 413 The spatially continuous AOD is also derived from level 2 aerosol products of MODIS Terra  
 414 and Aqua satellites (combined Dark Target, Deep Blue AOD at 0.55 micron, Collection 6.1,  
 415 Platnick et al., 2015). It provides a measure of the AOD at 550 nm during daytime for clear  
 416 sky conditions, with a spatial resolution of 10 km. To compare simulated AOD from WRF-  
 417 CHIMERE models with AOD from MODIS, the former is converted from 600 nm to 550 nm.  
 418 The conversion is performed using the Ångström formula (eq. 2).

419  
 420 Table 3 provides a general overview of the data used to evaluate the simulations in this  
 421 study.

422  
 423 **Table 3** - Summary of data used to evaluate the simulations.

product	type	resolution
Zagtouli solar farm monitoring system	pyranometer GHI measurement	local

<b>GHI</b>	AMMA-CATCH observational network	pyranometer GHI measurement	local
	CAMS gridded solar radiation	atmospheric reanalysis	0.01°x0.01°
<b>temperature</b>	INDAAF network	ground measurements	local
	ERA5	atmospheric reanalysis	0.25°x0.25°
<b>PM<sub>10</sub></b>	INDAAF network	ground measurements	local
	CAMS (v48R1, EAC4)	atmospheric reanalysis	0.75°x0.75°
<b>Aerosol Size Distribution</b>	AERONET network	inversion product	local
<b>Aerosol Optical Depth</b>	AERONET network	sunphotometer ground measurements	local
	MODIS	satellite observations	10km

424

425

### 3. Results

426

427

428

429

430

431

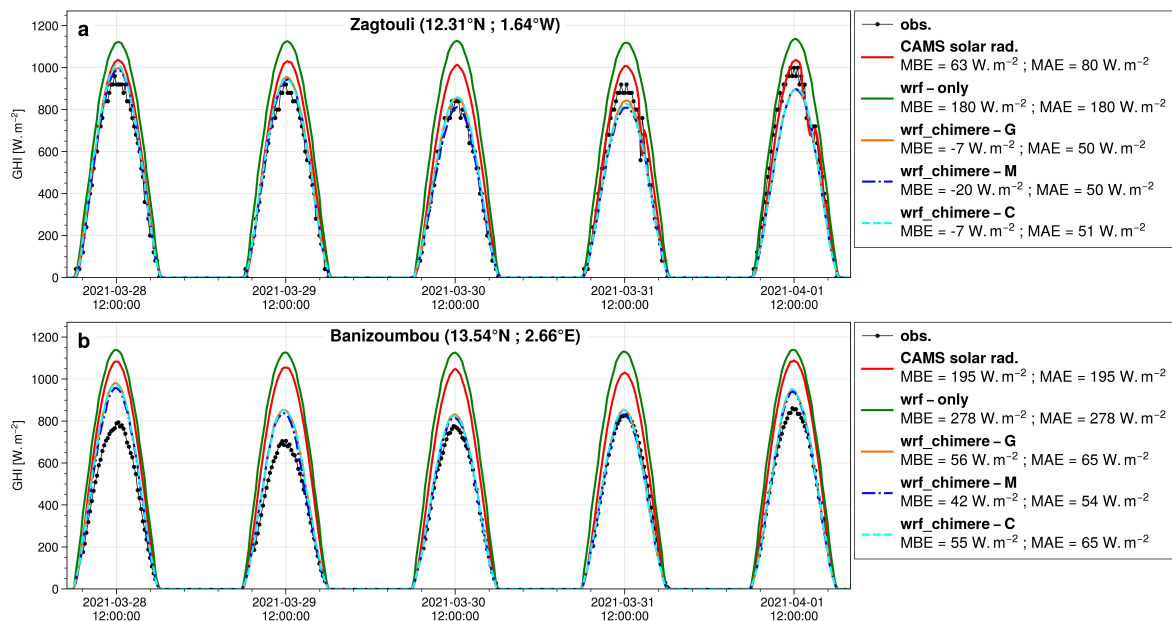
432

433

434

The analysis starts by assessing the errors and uncertainties associated with the dust aerosol initial and boundary condition dataset employed to estimate the variables of interest for solar production, i.e. GHI and surface temperature. Subsequently, we investigate the potential causes of these uncertainties by evaluating the AOD, aerosol size distribution, and surface aerosol concentration (PM<sub>10</sub>), as well as by examining mineral dust emissions and the flux of these aerosols at the boundaries of the domain. The metrics used to assess the quality of the simulations are described in Supplementary Materials.

#### 3.1. GHI



435

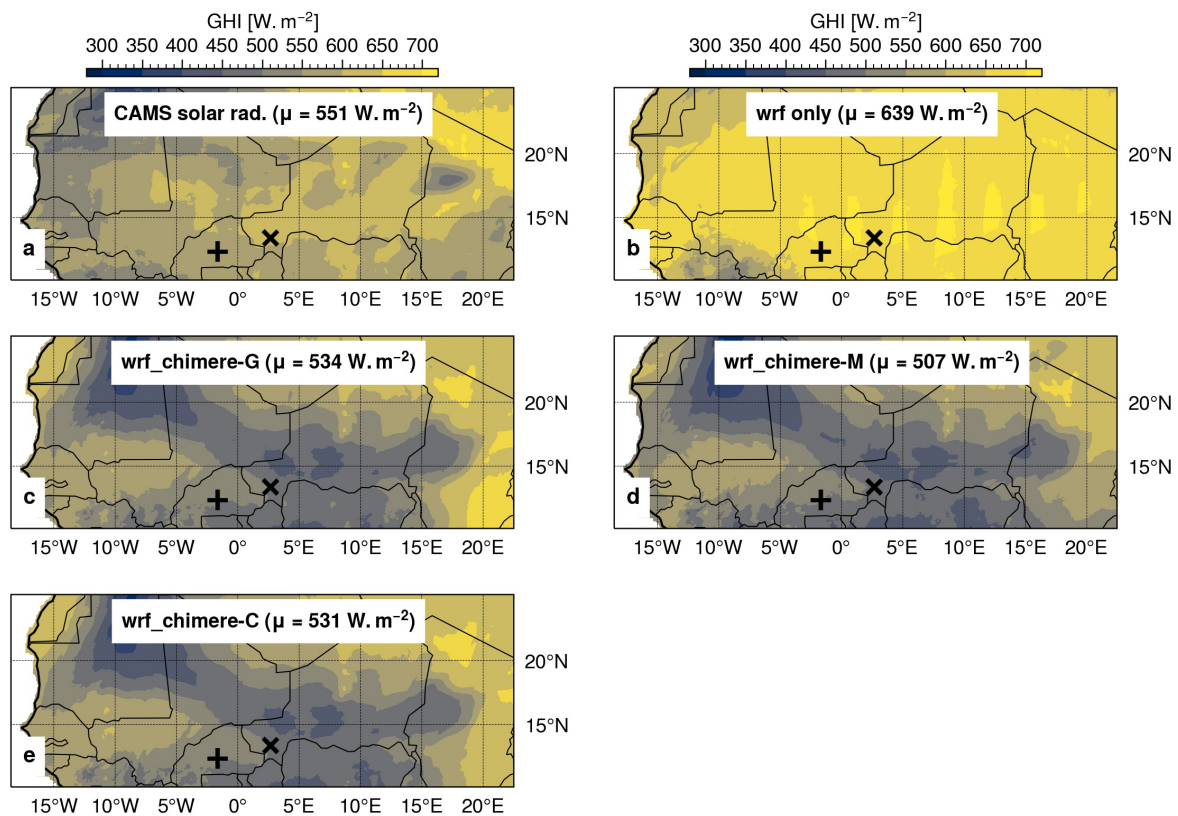
436 **Figure 2** - Local comparison of CAMS gridded solar radiation product and simulated GHI  
 437 against a) the Zagtouli solar farm observations and b) the Banizoumbou AMMA-CATCH  
 438 observations. *wrf\_chimere-G*, *wrf\_chimere-M* and *wrf\_chimere-C* refer to the WRF-  
 439 CHIMERE simulations using GOCART, MERRA2 and CAMS as dust aerosol initial and  
 440 boundary condition dataset respectively.

441  
 442 In Fig. 2, the local evaluation demonstrates the effect of taking into account dust aerosol for  
 443 GHI estimation with the WRF-CHIMERE coupling over the WRF meteorological model  
 444 alone. The coupling reduces the MAE by a factor of 3.6 at Zagtouli and by a factor of 4.6 at  
 445 Banizoumbou on average. The simulations accurately represent the reduction in GHI  
 446 intensity caused by the dust plume at both stations. However, the reduction persists  
 447 compared to the observations at Zagtouli. At Banizoumbou, the simulations overestimate  
 448 GHI at the beginning and end of the case study.

449 Figure 2 also indicates that the CAMS gridded solar radiation product fails to fully reproduce  
 450 the dust event, with only a small reduction in GHI during the passage of the dust plume and  
 451 an intermediate MAE between the WRF only and the WRF-CHIMERE simulations. This point  
 452 serves to highlight the advantages of using a regional model in comparison to a global  
 453 product for the simulation of dust conditions and the estimation of solar irradiance.

454 Furthermore, the uncertainty in GHI estimation related to the choice of the dust aerosol initial  
 455 and boundary condition dataset is limited, particularly when compared to the errors. This is  
 456 evidenced by the fact that the mean standard deviation between the three WRF simulations  
 457 is only 7% of the average MAE of these simulations at Zagtouli, and only 5% at  
 458 Banizoumbou.

459



460  
 461 **Figure 3** - Mean day-time GHI during the period of 28 March-00 UTC to 02 April-00 UTC  
 462 2021 as estimated by a) the CAMS gridded solar radiation dataset, b) the WRF only

463 simulation, and the WRF-CHIMERE simulations with c) GOCART, d) MERRA2 and e)  
464 CAMS as dust aerosol initial and boundary condition dataset; + is the Zagtouli solar farm  
465 and x is the Banizoumbou site.  $\mu$  is the mean GHI estimates over the domain.

466

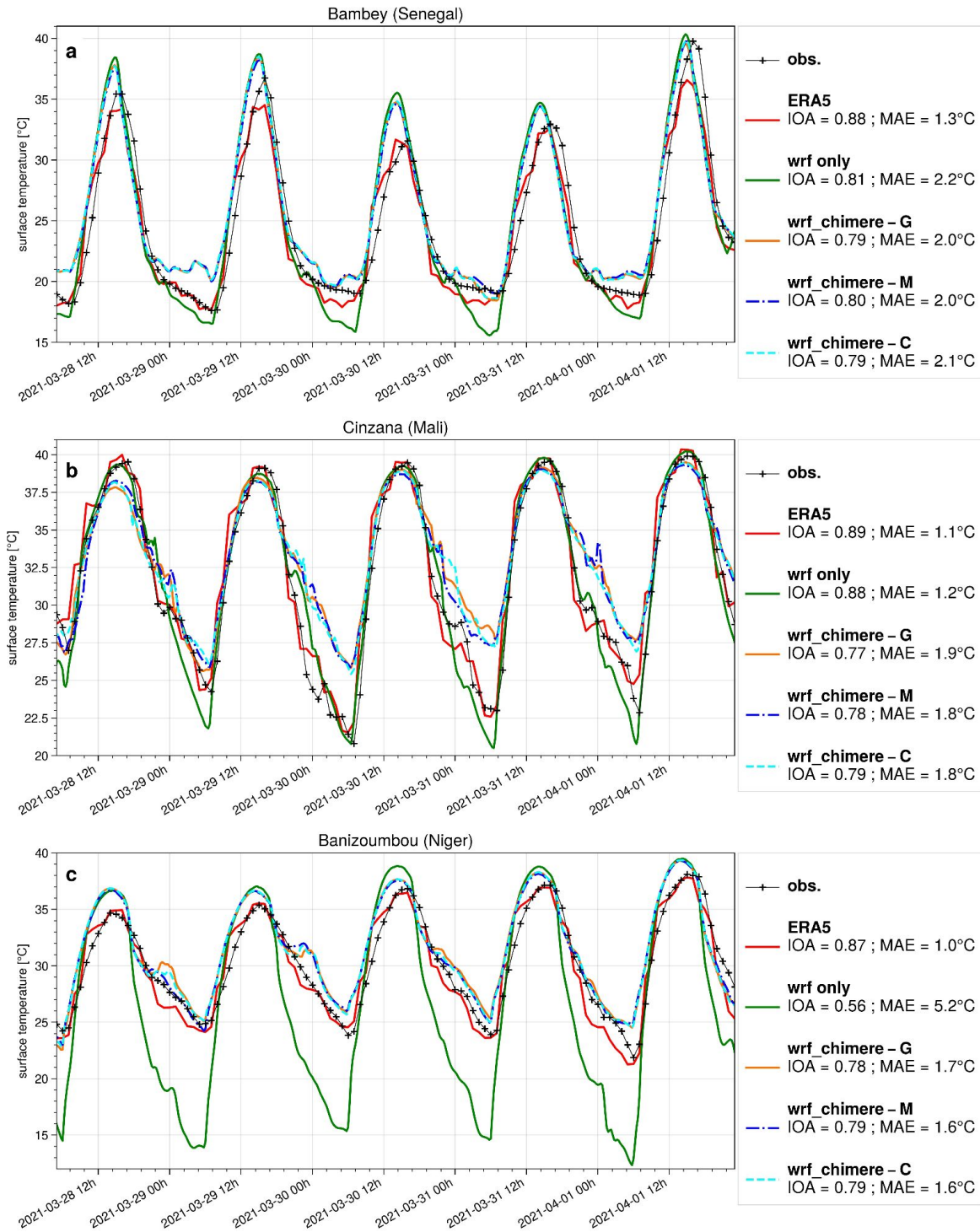
467 The regional comparison presented in Fig. 3 provides more insight into the impact of  
468 incorporating dust on GHI estimation with the WRF-CHIMERE coupling, when compared to  
469 the WRF meteorological model alone. As anticipated the WRF-only simulation has the  
470 highest GHI estimates. The WRF-CHIMERE simulations indicate that dust aerosols reduce  
471 the mean GHI estimation by approximately  $115 \text{ W} \cdot \text{m}^{-2}$  (-18%) as compared to the WRF-only  
472 simulation, while the CAMS gridded solar radiation global product shows a reduction of  
473  $88 \text{ W} \cdot \text{m}^{-2}$  (-14%). The three WRF-CHIMERE simulations exhibit identical regional patterns,  
474 with lower mean GHI values observed on the dust plume trajectory from the Bodélé  
475 Depression to the West, and also in the South Atlas region. In contrast, the CAMS gridded  
476 solar radiation dataset does not show this regional pattern, which may indicate that this  
477 global product does not fully capture the dust event.

478 Furthermore, the uncertainty in GHI estimation associated with the choice of the dust aerosol  
479 initial and boundary conditions dataset is limited, particularly when compared to the changes  
480 brought by the taking of dust aerosol into account. Indeed, the standard deviation between  
481 the three WRF-CHIMERE simulations represents only 5% of the mean difference between  
482 these three simulations and the WRF-only simulation without dust.

483

484

### 3.2. Temperature



485  
 486 **Figure 4** - Local comparison of ERA5 and simulated surface temperature with the INDAAF  
 487 observations for a) Bambey (Senegal), b) Cinzana (Mali) and c) Banizoumbou (Niger)  
 488 measurement sites. *wrf\_chimere-G*, *wrf\_chimere-M* and *wrf\_chimere-C* refer to the WRF-  
 489 CHIMERE simulations using GOCART, MERRA2 and CAMS as dust aerosol initial and  
 490 boundary condition dataset respectively. *IOA* is the Indicator of Agreement and *MAE* is the  
 491 Mean Absolute Error.

492  
 493 Figure 4 illustrates the contrasting outcomes of taking into account dust aerosols into the  
 494 WRF-CHIMERE coupling in comparison to the WRF meteorological model alone for the



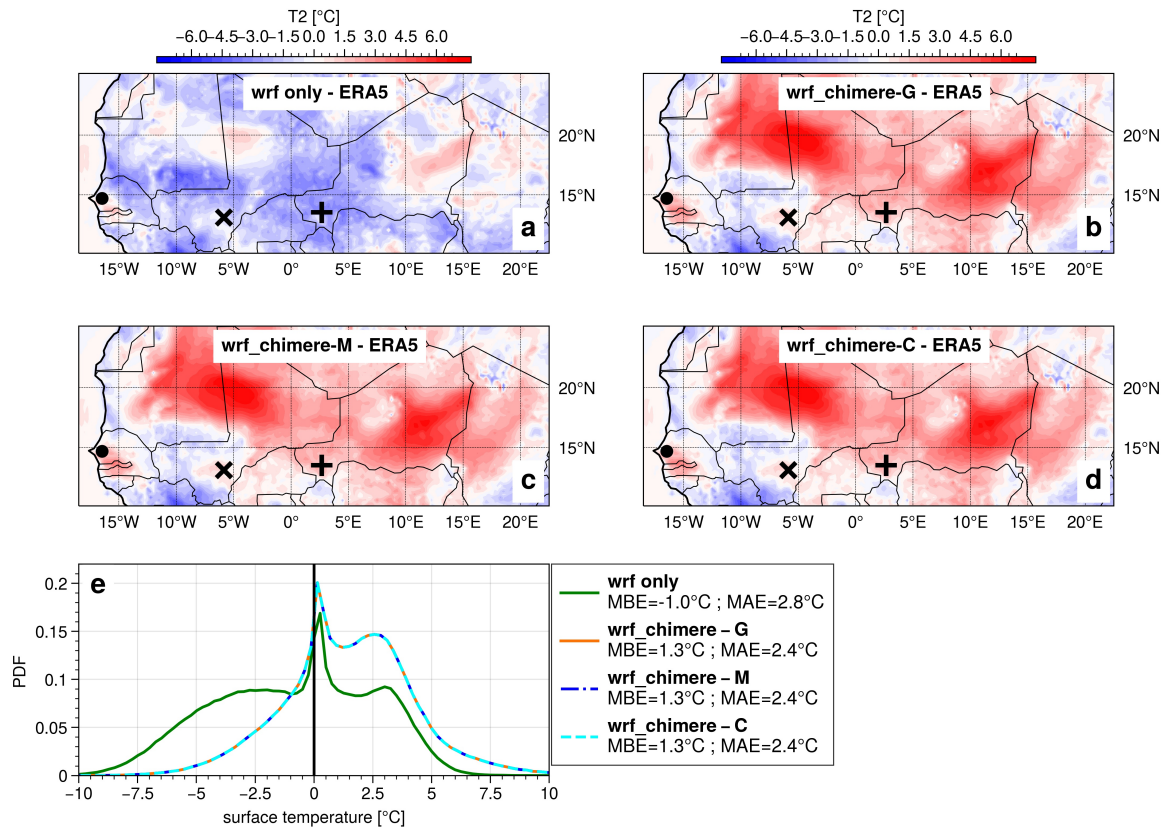
495 estimation of surface temperature. At Bambey (Fig. 4a), which is far from the dust source  
496 areas, the coupling has no effect on daytime temperatures but does affect night-time  
497 temperatures. The WRF-CHIMERE and WRF-only simulations have IOA and MAE of the  
498 same order of magnitude. At Cinzana (Fig. 4b), the WRF-only simulation performed better,  
499 with a MAE 0.6°C lower than the coupled simulations, especially for night-time temperatures  
500 but also for estimating the daily temperature peak. Finally, at Banizoumbou (Fig. 4c), which  
501 is near the dust source areas, the coupling leads to a significant improvement in surface  
502 temperature estimation, with an IOA of approximately 0.79 compared to 0.56 for the WRF-  
503 only simulation and a MAE reduced by around 3.6°C. The impact of dust aerosols on  
504 temperature is particularly pronounced at night-time. However, dust also affects the daily  
505 temperature peak, with a reduction of 1.1°C of the daily maximum temperature observed on  
506 the 30th of March.

507 Depending on the position of the measurement station, the results show a contrast, with a  
508 significant improvement with the model coupling close to the source zones at Banizoumbou.  
509 However, this improvement is reversed with increasing distance at Cinzana. This suggests  
510 errors in the simulation of the transport of the dust plume from the source zones (Bodélé  
511 Depression) towards the West. Overall, the main differences between WRF only and WRF-  
512 CHIMERE coupled simulations occur at night time when there is no solar production. These  
513 differences highlight the warming effect due to the dust aerosol interaction with the longwave  
514 earth radiation.

515 In general, the uncertainty associated with the choice of the dust aerosol initial and boundary  
516 condition dataset for the WRF-CHIMERE simulations is negligible compared to the errors in  
517 temperature estimation or the difference with the WRF-only simulation.

518 The value of the ERA5 reanalysis for surface temperature evaluation is also reinforced in  
519 Fig. 4, since it shows the lowest MAE and highest IOA. This dataset can therefore be  
520 considered reliable for a regional evaluation of surface temperature.

521



522  
 523 **Figure 5** - Mean difference in surface temperature as compared to the ERA5 reanalysis for  
 524 a) the WRF only simulation, the WRF-CHIMERE simulations with b) GOCART, c) MERRA2  
 525 and d) CAMS as dust aerosol initial and boundary condition dataset, during the period of 28  
 526 March-00 UTC to 02 April-00 UTC 2021; the black point is the Bambey, x is the Cinzana and  
 527 + is the Banizoumbou INDAAF sites. e) Probability Density Function for the differences in  
 528 surface temperature between simulations and the ERA5 reanalysis.

529  
 530 The regional surface temperature evaluation in Fig. 5 also reveals a contrast benefit of the  
 531 coupling approach for the surface temperature estimation. While the WRF alone simulation  
 532 (Fig. 5a) underestimates the surface temperature all over the domain, WRF-CHIMERE  
 533 simulations are overestimating surface temperature in the dusty areas (Saharan region, Fig.  
 534 5bcd). Overall, taking into account dust aerosol in the estimation of surface temperature  
 535 reduces the MAE by 14% (Fig. 5e) when comparing the surface temperature estimates from  
 536 simulations with the ERA5 reanalysis.

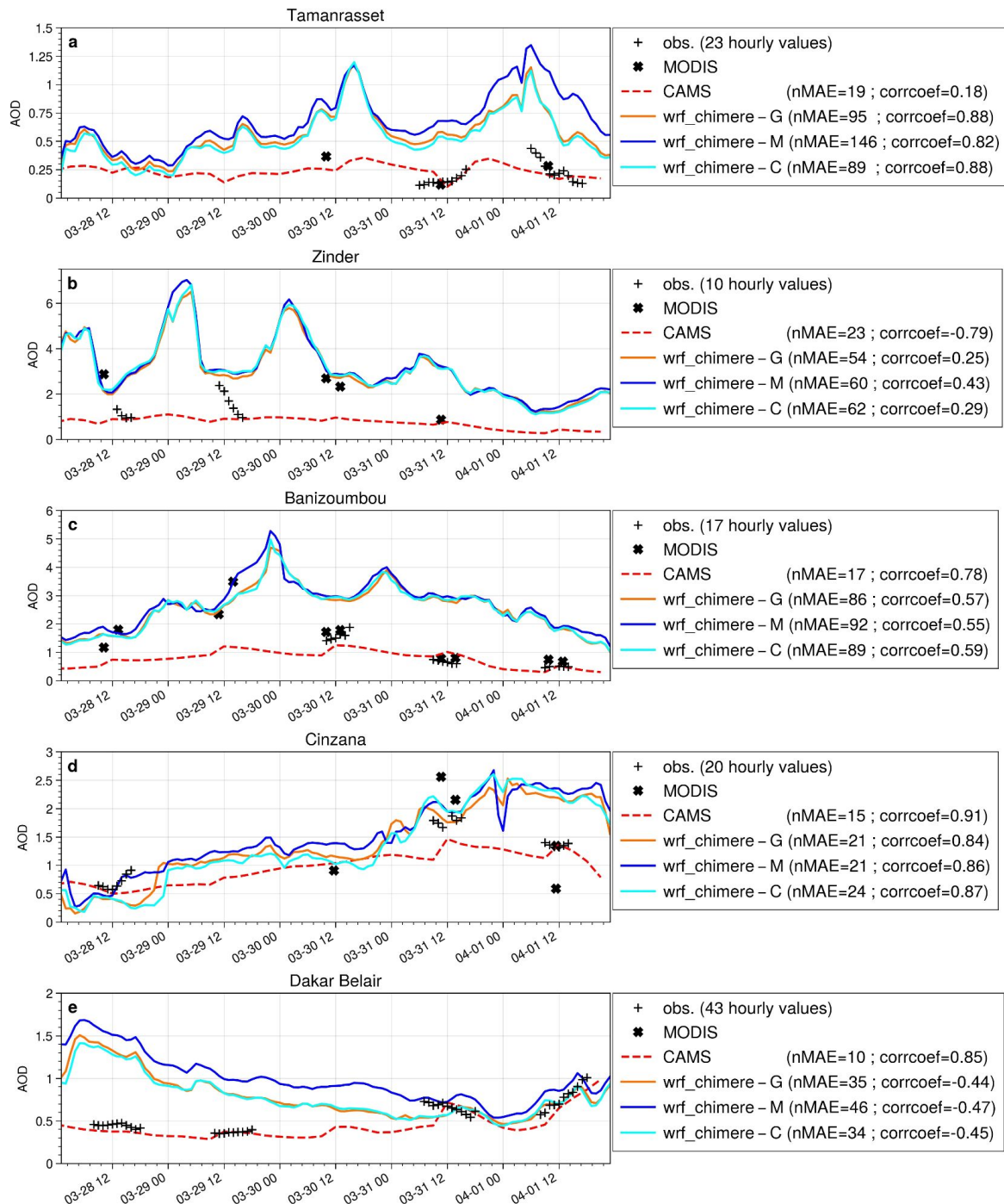
537 Furthermore, the uncertainty associated with the choice of the dust aerosol initial and  
 538 boundary conditions dataset is limited. This is demonstrated by the fact that the standard  
 539 deviation between the three WRF-CHIMERE simulations averaged over the period of  
 540 analysis is 12% of the mean bias of those three simulations in comparison to ERA5  
 541 reanalysis, and only 7% of the difference between the coupled simulations and the WRF-  
 542 only simulation without dust.

543  
 544 Finally, the incorporation of dust aerosol into the estimation of GHI appears to be a crucial  
 545 element in this case study. However, the value of this approach is more debatable in the  
 546 context of surface temperature estimation. Furthermore, the uncertainty related to the dust  
 547 aerosol initial and boundary condition dataset selection is limited, particularly when

548 compared to the simulation errors, and to the differences between including dust in the  
 549 simulation and not including it. The following sections will examine the simulated dust  
 550 aerosol condition during the case study in order to explain the discrepancies observed in  
 551 GHI and surface temperature, which are key parameters for solar production.  
 552

553

### 3.3. Aerosol Optical Depth



554

555 **Figure 6** - Local comparison of simulated AOD with AERONET in-situ measurements at 440  
 556 nm for a) Tamanrasset, b) Zinder, c) Banizoumbou, d) Cinzana and e) Dakar Belair stations.  
 557 *wrf\_chimere-G*, *wrf\_chimere-M* and *wrf\_chimere-C* refer to the WRF-CHIMERE simulations  
 558 using GOCART, MERRA2 and CAMS as dust aerosol initial and boundary condition dataset

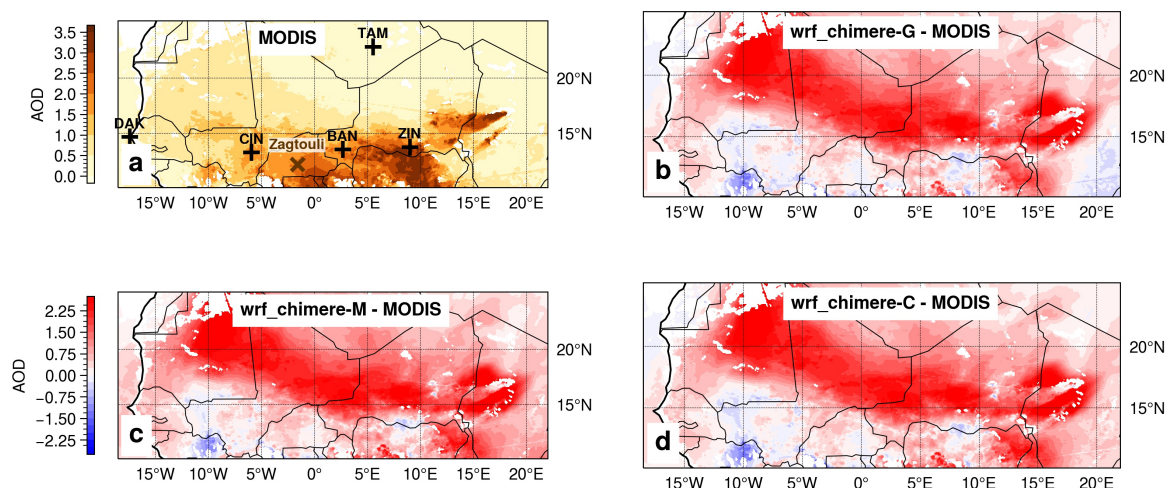
559 respectively; *MODIS* and *CAMS* refer to the AOD at 440 nm from the MODIS satellite  
 560 observations and the CAMS atmospheric reanalysis respectively. *nMAE* is the normalised  
 561 mean absolute error in % and *corrcoef* is the Pearson correlation coefficient, both derived  
 562 with AERONET measurements as the reference.

563

564 The local evaluations presented in Figure 6 reveal an overestimation of the AOD for stations  
 565 close to dust sources such as Tamanrasset ( Fig. 6a), Zinder ( Fig. 6b) and Banizoumbou  
 566 ( Fig. 6c). This overestimation is more limited with increasing distance from the dust source  
 567 at Cinzana (Fig. 6d) and Dakar (Fig. 6e). The order of magnitude of the dispersion between  
 568 the three simulations is small when compared to the errors of the simulation in representing  
 569 the observed AOD. As a consequence, the uncertainty associated with the choice of the dust  
 570 aerosol initial and boundary condition dataset is limited. Overall, the AERONET AOD  
 571 measurements appear to be very scarce, particularly close to the dust aerosol sources  
 572 (Zinder, Tamanrasset, Banizoumbou, Cinzana). The AOD measurements are performed by  
 573 sun photometers which give recording by pointing at the sun. Thus these recordings are only  
 574 available during daytime and with clear sky conditions. In some cases of intense dust  
 575 plumes with very high concentration, leading to strong solar radiation absorption, the sun  
 576 photometers are technically limited and cannot produce any record or, sometimes, the  
 577 AERONET quality control system removes them (Mueller et al., 2015 ; Giles et al., 2019).  
 578 This may be the reason for the scarcity of observations in this case study, which focuses on  
 579 an intense dust event, increasing the perceived overestimation of the simulations. To  
 580 compensate for this, the AOD estimates from MODIS satellite observations have been  
 581 added to Figure 6 to complete the data.

582 Furthermore, the CAMS reanalysis appears to be a reliable dataset for dust AOD estimation,  
 583 as it has no overestimation and has the lowest *nMAE* for all sites. Although it does not  
 584 reproduce the AOD dynamics close to the dust source at Tamanrasset and Zinder, it has the  
 585 highest correlation coefficient for the other sites. Nevertheless, this result should be  
 586 interpreted with caution, given the limited data available for calculating the dataset  
 587 evaluation metrics. More research is needed to substantiate this conclusion.

588



589

590 **Figure 7** - a) Mean from March 28th-00 UTC to April 2nd-00 UTC 2021 of MODIS AOD at  
 591 550 nm satellite observations; x is the Zagtoui solar farm and + corresponds to AERONET  
 592 stations. For panels b, c and d, AOD at 550 nm mean differences from March 28th-00 UTC

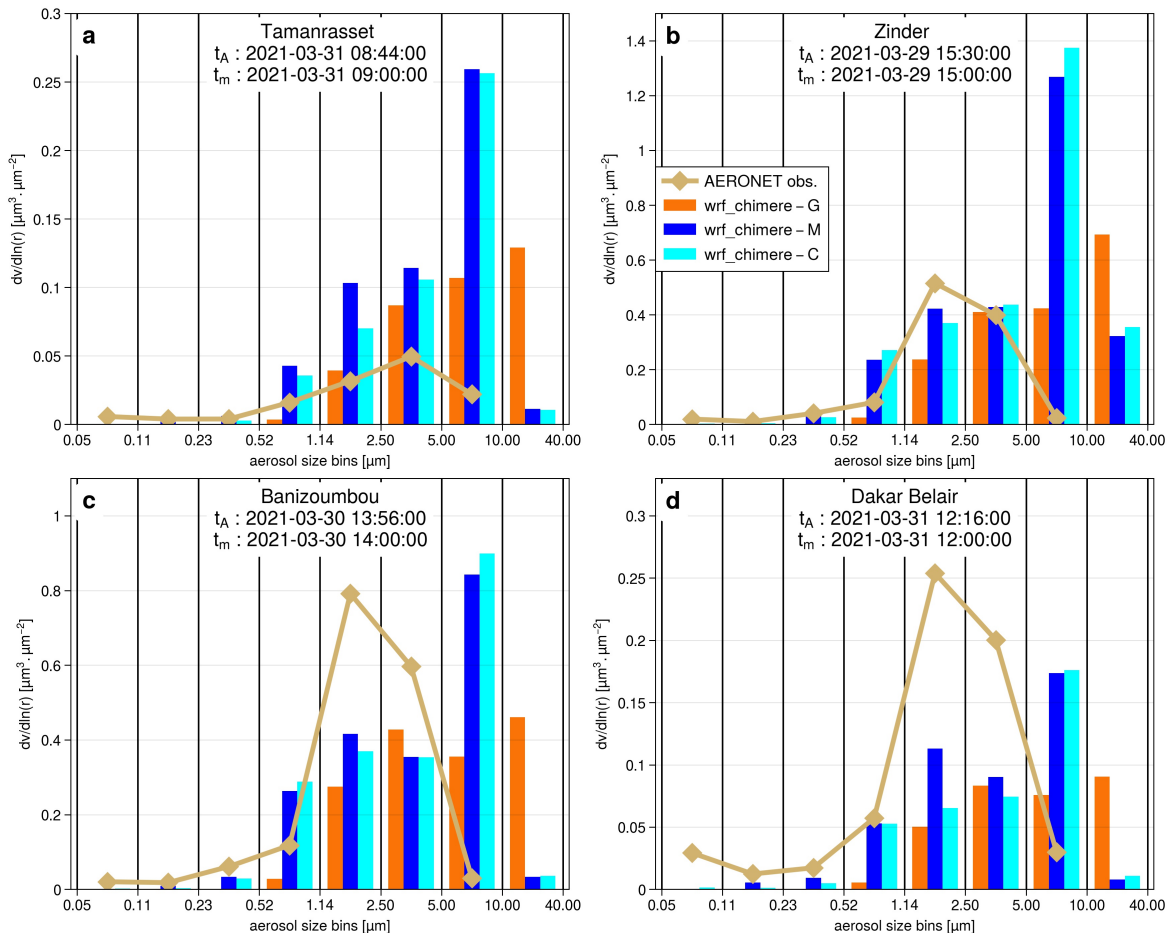
593 to April 2nd-00 UTC 2021 between each of the WRF-CHIMERE simulations driven by  
 594 GOCART, MERRA2 and CAMS, respectively, and the MODIS satellite observations.  
 595

596 The AOD differences shown in Fig. 7bcd show that the simulations significantly overestimate  
 597 the AOD as compared to the MODIS satellite observations, particularly in the Saharan and  
 598 North Sahelian zones and in the South Atlas, with an average overestimation of +1.25  
 599 between 15°N and 20°N. It is important to note that this overestimation is localised close to  
 600 the desert aerosol source zones. The simulated AOD error in the Sahel zone, particularly  
 601 around the Zagtouli solar power plant, is more limited with an average of +0.51 between  
 602 10°N and 15°N. The mean standard deviation between the three WRF-CHIMERE  
 603 simulations is only 10% of the mean error and 5% of the mean simulated AOD.  
 604 Consequently the uncertainty in the AOD estimate associated with the selection of the dust  
 605 aerosol initial and boundary condition dataset is small.

606 The observed overestimation of AOD by the WRF-CHIMERE simulations could be due to an  
 607 overestimation of the aerosol concentration, or to an inaccurate estimation of the size  
 608 distribution of the dust plume, or to excessive aerosol emissions within the domain, or to an  
 609 excessive inflow of desert aerosols at the domain boundaries. These hypotheses are  
 610 investigated below. Another potential explanation may also be the uncertainties in the  
 611 radiative properties of the dust aerosol incorporated in the CHIMERE model, or an  
 612 underestimation of the aerosol deposition flux; these aspects are not investigated here.  
 613

614

### 3.4. Aerosol size distribution



615  
 616

**Figure 8** - Aerosol volume size distribution for the AERONET station located in a)

617 Tamanrasset, b) Zinder, c) Banizoumbou and d) DakarBelair.  $t_A$  and  $t_m$  indicate the times of  
618 the AERONET inversion product and the WRF-CHIMERE model respectively used for the  
619 comparison. *wrf\_chimere-G*, *wrf\_chimere-M* and *wrf\_chimere-C* refer to the WRF-CHIMERE  
620 simulations using GOCART, MERRA2 and CAMS as dust aerosol initial and boundary  
621 condition dataset respectively.

622

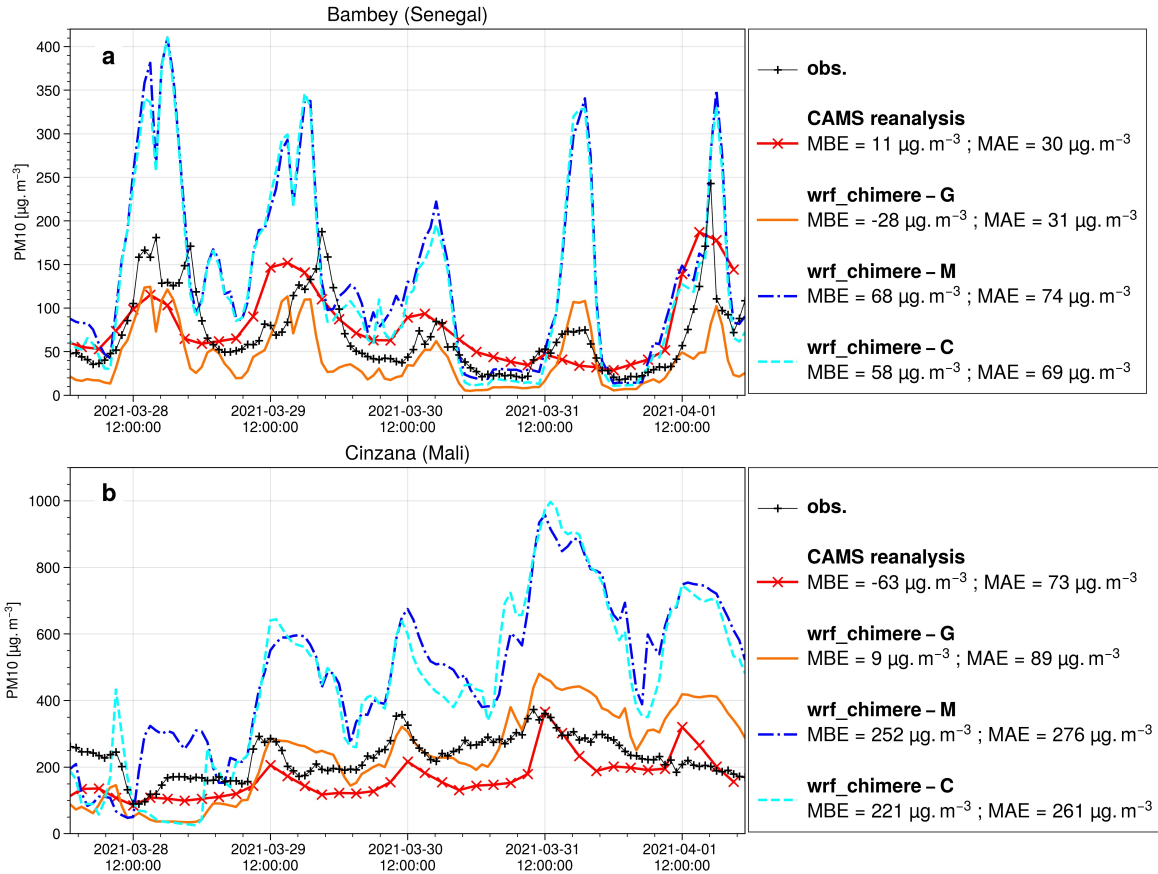
623 The evaluation of the aerosol size distribution in Fig. 8 shows that the simulations generally  
624 have a dominant aerosol size mode shifted towards coarser sizes compared to the  
625 AERONET inversion product. The ground-based size distribution has a strong peak between  
626 1.14  $\mu\text{m}$  and 5.00  $\mu\text{m}$ , whereas the size distributions estimated by the WRF-CHIMERE  
627 simulations peak for coarser aerosol. For the Dakar Belair station (Fig. 8d), the AERONET  
628 inversion product indicates a first peak of lower intensity between 0.05 and 0.11  $\mu\text{m}$ , which  
629 suggests the presence of aerosols other than desert dust. These aerosols may be of  
630 anthropogenic origin, given the proximity of the measurement site to the Senegalese capital.  
631 When comparing the size distributions between the three simulations with different dust  
632 aerosol initial and boundary condition dataset, it can be seen that the simulations driven with  
633 CAMS and MERRA2 reanalysis are relatively close and well separated from the one driven  
634 with the GOCART climatology. Notably, the dominant size bin in the simulation using  
635 GOCART dataset is consistently the largest particles, whereas with the aerosol from  
636 reanalyses, it is the aerosols between 5  $\mu\text{m}$  and 10  $\mu\text{m}$ . Consequently, the uncertainty  
637 associated with the selection of the dust aerosol initial and boundary condition dataset is  
638 high when examining the aerosol size distribution, particularly for particles exceeding 5.00  
639  $\mu\text{m}$  in diameter. The aforementioned uncertainties in the aerosol size distribution, which are  
640 linked to the choice of the dust aerosol initial and boundary conditions dataset, may be  
641 attributed to differences in the flow of desert dust entering the domain, as well as  
642 uncertainties in the transfer method carried out by the CHIMERE model to match the aerosol  
643 classes of these datasets to its own size distribution, described in section 2.2.3.

644 As a result, the shift in the WRF-CHIMERE size distribution towards coarser particles  
645 compared to AERONET observations would result in a simulated AOD smaller than  
646 AERONET measurements. However, the opposite is observed (section 3.3). This suggests a  
647 positive bias in the simulated aerosol concentration, which would explain the positive bias in  
648 the AOD, while the coarser size distribution would tend to compensate.

649

650

### 3.5. Aerosol concentrations

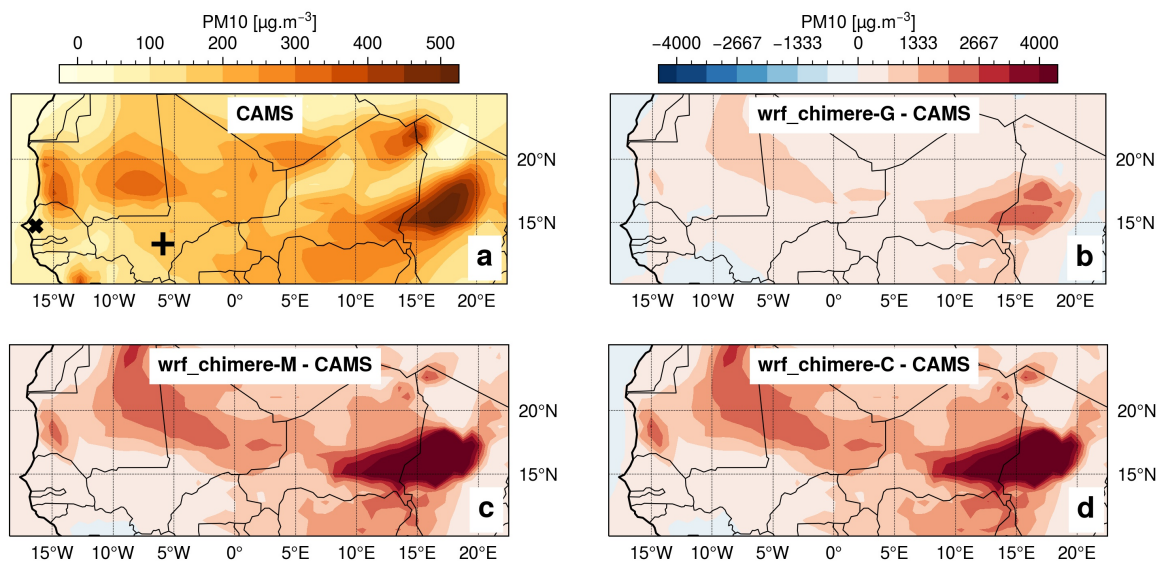


651  
652 **Figure 9** - Local comparison of CAMS reanalysis and simulated PM<sub>10</sub> surface concentrations  
653 with INDAAF network observations for a) Cinzana and b) Bambeey stations. *wrf\_chimere-G*,  
654 *wrf\_chimere-M* and *wrf\_chimere-C* refer to the WRF-CHIMERE simulations using GOCART,  
655 MERRA2 and CAMS as dust aerosol initial and boundary condition dataset respectively.  
656 MBE is the mean bias error and MAE refers to the mean absolute error.

657  
658 The three simulations properly capture the dynamics of the PM<sub>10</sub> surface concentration with  
659 respect to the INDAAF ground measurement (Fig. 9) as correlation coefficients are around  
660 0.6 at Cinzana and close to 0.7 at Bambeey. The WRF-CHIMERE simulations driven with  
661 MERRA2 and CAMS dust aerosol datasets overestimate the surface PM<sub>10</sub> concentration  
662 peaks for Bambeey (Fig. 9a) and Cinzana (Fig. 9b), with high positive bias values of around  
663 63 g.m<sup>-3</sup> at Bambeey and 247 g.m<sup>-3</sup> at Cinzana. The latter station is closer to the dust  
664 aerosol sources. In contrast, the simulation using the GOCART dust aerosol dataset  
665 demonstrates superior performance in representing this variable, with an MAE that is  
666 approximately 60% and 70% lower than the two other simulations at Bambeey and Cinzana,  
667 respectively.

668 Furthermore, the uncertainty associated with the selection of initial and boundary condition  
669 dataset for dust aerosols is of a comparable magnitude to the simulation errors observed for  
670 surface PM<sub>10</sub> concentrations. Section 3.4 partly explains these discrepancies in surface PM<sub>10</sub>  
671 concentration estimates between the simulation driven with the GOCART climatology and  
672 those driven with CAMS or MERRA2 reanalysis in terms of aerosol size distribution. These  
673 differences may also be attributed to variations in the size distribution of dust aerosol  
674 emissions or in the inflow of dust into the simulation domain and its aerosol size distribution.

675 Furthermore, Fig. 9 indicates that the CAMS reanalysis provides reliable estimates of  
 676 surface PM<sub>10</sub> concentration, as evidenced by the fact it has the lowest MAE values.  
 677 However, the Bambey and Cinzana ground measurements, which are the only two available  
 678 for the case study, are situated at a considerable distance from the dust sources, limiting our  
 679 ability to assess the accuracy of the CAMS reanalysis in capturing the dust event. Moreover,  
 680 the CAMS reanalysis exhibits a negative bias at Cinzana, which is the closest site to the dust  
 681 sources.  
 682



683  
 684 **Figure 10** - a) Mean from March 28th-00 UTC to April 2nd-00 UTC 2021 of CAMS reanalysis  
 685 PM<sub>10</sub> surface concentration; x refers to the Bambey and + corresponds to Cinzana INDAAF  
 686 stations. For panels b, c and d, PM<sub>10</sub> surface concentration mean differences from March  
 687 28th-00 UTC to April 2nd-00 UTC 2021 between each of the WRF-CHIMERE simulations  
 688 driven by GOCART, MERRA2 and CAMS, respectively, and the CAMS reanalysis.  
 689

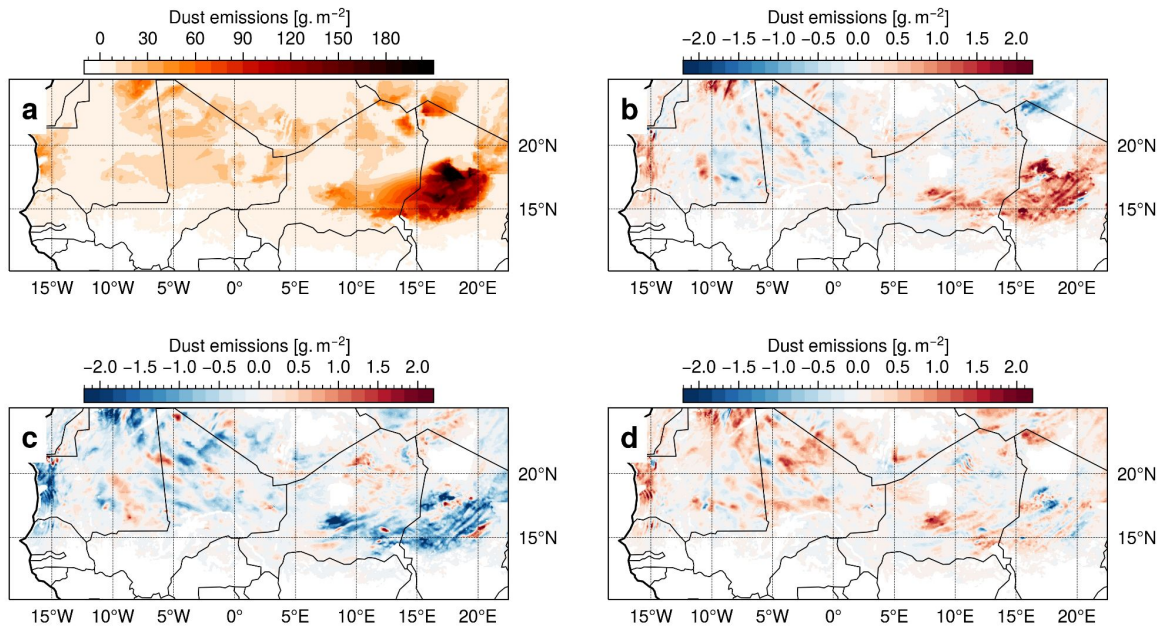
690 Figure 10 illustrates an overestimation of the PM<sub>10</sub> concentrations as compared to the CAMS  
 691 reanalysis. This is particularly evident in dust source areas such as the Bodélé Depression.  
 692 The WRF-CHIMERE simulation driven with the GOCART dataset is the closest to the CAMS  
 693 reanalysis, with a mean estimate 3.6 times higher. However, this ratio reaches 8.6 for the  
 694 simulations driven with the CAMS and MERRA2 reanalysis dataset.

695 The mean standard deviation between the three WRF-CHIMERE simulations is 35% of their  
 696 mean PM<sub>10</sub> surface concentration estimate. Consequently the uncertainty in the estimation of  
 697 dust PM<sub>10</sub> surface concentration associated with the selection of the dust aerosol initial and  
 698 boundary condition dataset is significant. The discrepancies between the simulation using  
 699 the GOCART climatology and the two other ones using CAMS or MERRA2 reanalysis can  
 700 be partly explained by the differences in the simulated aerosol size distribution, as shown in  
 701 section 3.4.

702  
 703

### 3.6. Dust emissions



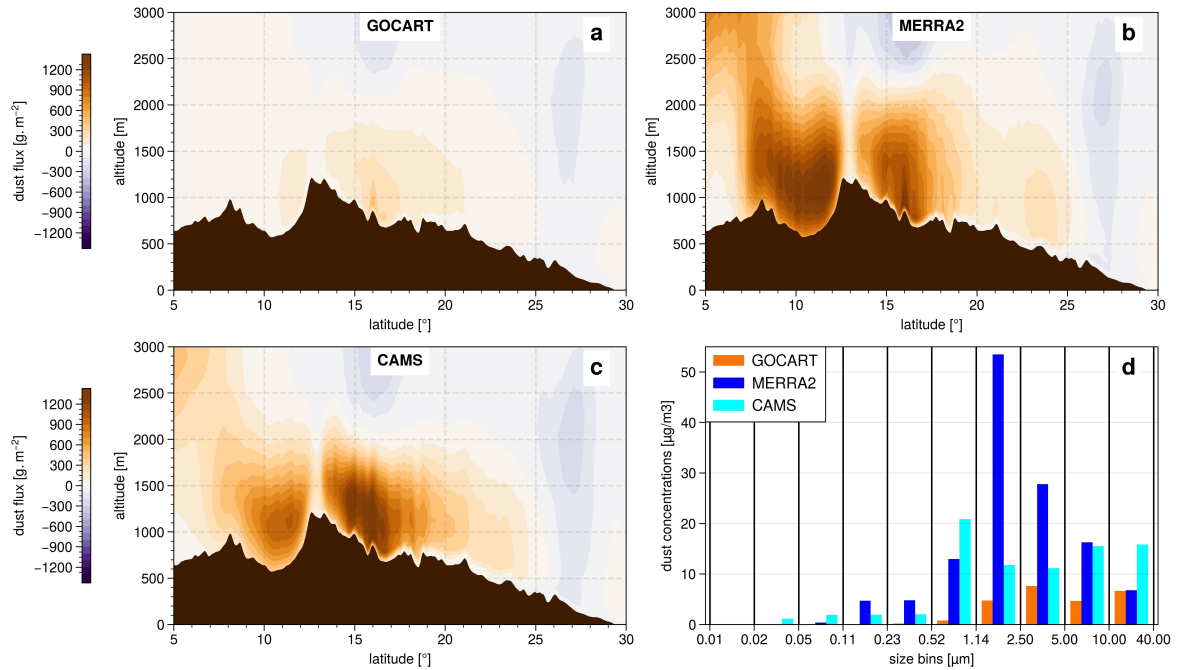


704  
 705 **Figure 11** - a) Total dust emissions flux from March 28th-00 UTC to April 2nd-00 UTC 2021,  
 706 averaged between the three WRF-CHIMERE simulations. For panels b, c and d, total dust  
 707 emissions individual differences between each of the WRF-CHIMERE simulations driven by  
 708 GOCART, MERRA2 and CAMS, respectively, and the mean of the three WRF-CHIMERE  
 709 simulations.

710  
 711 In terms of dust emissions (Fig. 11), the Bodélé Depression is, as expected, identified as  
 712 the primary dust source area, with emissions reaching up to 244 g/m<sup>2</sup>. The differences of the  
 713 simulations with each of the three dust aerosol initial and boundary conditions dataset,  
 714 relative to their mean, exhibit highest values in the source zones located at the Bodélé  
 715 Depression and the South Atlas. Nevertheless, it is worth noting that there is a factor of 100  
 716 in between the emissions in the Bodélé area (approximately 200g/m<sup>2</sup>) and the observed  
 717 differences between the three simulations. Consequently, the uncertainties in dust emissions  
 718 resulting from the choice of the dust aerosol initial and boundary conditions dataset can be  
 719 considered negligible. As emissions are primarily influenced by surface wind, it can be  
 720 inferred that the uncertainty generated by the dust aerosol driving dataset on the surface  
 721 wind is negligible too, which is confirmed by Fig. S4. Additionally, the size distributions of the  
 722 aerosols emitted during the case study are found to be identical (not shown). Therefore, the  
 723 differences in dust surface concentration and dust aerosol size distribution may be partly  
 724 attributed to the dust flows at the boundaries of the domain and are not linked to differences  
 725 in simulated dust emissions within the domain. However, there is no observational data  
 726 available to enable a quantitative evaluation of the accuracy of the emissions computed  
 727 within the WRF-CHIMERE simulations.

728  
 729

### 3.7. Dust boundary flux



730  
 731 **Figure 12** - Cumul of the dust flux at the eastern boundary of the simulation from March  
 732 28th-00 UTC to April 2nd-00 UTC 2021 for the WRF-CHIMERE simulation with a) GOCART,  
 733 b) MERRA2 and c) CAMS as dust aerosol initial and boundary conditions dataset; d) Dust  
 734 size distribution at the eastern boundary limit average during the case study period, from the  
 735 surface to 200hPa and over latitude. In panel abc, the dust flux is derived as the product  
 736 between the dust aerosol concentration and the zonal wind, and positive values of the dust  
 737 flow indicate a flow entering the simulation domain.

738  
 739 As shown in Fig. 1b, the dust event is associated with a strong Harmattan flow,  
 740 characterised by a northeasterly flow in the lower layer. It is thus interesting to quantify the  
 741 dust inflow associated with each of the dust aerosol initial and boundary conditions dataset  
 742 for the eastern domain boundary. The lowest dust flux is observed with GOCART (Fig. 12a),  
 743 with a maximum of approximately  $480 \text{ g/m}^2$ . In contrast, MERRA2 and CAMS (Fig. 14 b  
 744 and c respectively) exhibit higher dust fluxes, with maximum values of around  $1650 \text{ g/m}^2$ .  
 745 The maximum flow is around  $10^\circ\text{N}$  for MERRA2, while for CAMS, it is closer to  $16^\circ\text{N}$ . Given  
 746 that GOCART is a climatology, it is reasonable to expect a lower dust flux compared to the  
 747 CAMS and MERRA2 reanalyses, which are real case simulations incorporating data  
 748 assimilation of AOD. This is particularly true for the presented case study, which involves an  
 749 intense dust event associated with a Harmattan flow.

750 There are also significant differences in both quantity and distribution by aerosol size bin  
 751 (Fig. 12d). MERRA2 exhibits a strong dominant mode for the class between  $1.14 \mu\text{m}$  and  
 752  $2.50 \mu\text{m}$ , while CAMS shows significant values from  $0.52 \mu\text{m}$  to  $40 \mu\text{m}$ , with a maximum for  
 753 the size class between  $0.52 \mu\text{m}$  and  $1.14 \mu\text{m}$ . Finally, the GOCART model displays a lower  
 754 variability between  $1.14 \mu\text{m}$  and  $40.00 \mu\text{m}$ , with the maximum occurring for the size class  
 755 between  $2.55 \mu\text{m}$  and  $5.00 \mu\text{m}$ .

756 The eastern dust fluxes at the boundary significantly vary depending on the dataset used as  
 757 dust aerosol initial and boundary conditions, both in terms of quantity and size distribution.  
 758 The reanalysis dataset, CAMS and MERRA2, are expected to provide a more accurate  
 759 representation of dust flux in terms of quantity as they are real case simulations assimilating

760 observational data in their calculations, as compared to GOCART which is a climatology.  
761 However, GOCART provides a more comprehensive description of aerosol size distribution  
762 with seven classes, in comparison to CAMS, which has only three classes but proposes a  
763 higher horizontal resolution. While GOCART considers the effect of aerosol size to be  
764 essential, CAMS assumes the horizontal resolution to be a key parameter. MERRA2 is the  
765 most comprehensive of the three datasets, with the highest horizontal resolution, and an  
766 aerosol size distribution that is close to the GOCART one with five classes.  
767 As a result, and in consideration of the negligible uncertainty in dust emissions within the  
768 simulation domain related to the choice of the dataset for dust aerosol initial and boundary  
769 conditions (see 3.6), these differences in eastern dust fluxes appear to account for the  
770 uncertainties of the simulated surface dust concentrations (see 3.5) and dust aerosol size  
771 distribution (see 3.4).

772

### 773 **3.8. Discussions**

774 The evaluation of the simulated GHI at the Zagtouli solar power plant and the Banizoumbou  
775 site (Fig. 2) indicates a significant enhancement in surface solar irradiance estimation when  
776 WRF is coupled with CHIMERE. Specifically, the local MAE is reduced by approximately  
777 75%. This confirms the relevance of incorporating the dust radiative effect with a coupling  
778 approach, in comparison with the operational forecasts currently employed based on  
779 meteorological models alone. During the dry season, dust events similar to the one  
780 presented here, with emissions at Bodélé and then transport of the plume westwards, are  
781 common. This work therefore calls for forecasters in the photovoltaic sector to better account  
782 for the desert dust cycle in their forecast products. This local evaluation also highlights the  
783 potential benefits of using a regional model rather than a global product, as the WRF-  
784 CHIMERE simulations outperform the CAMS gridded solar radiation product with an average  
785 MAE reduced by approximately 38% at the Zagtouli solar farm and by 70% at the  
786 Banizoumbou site, which is closer to dust sources. These discrepancies are corroborated by  
787 the regional comparison presented in Figure 3, which reveals that the mean WRF-CHIMERE  
788 GHI estimate is 5% lower than the CAMS solar radiation dataset. Additionally, the latter does  
789 not exhibit a geographical pattern with lower GHI estimation along the dust plume trajectory,  
790 in contrast to the WRF-CHIMERE simulations. These results confirm those from Sawadogo  
791 et al. (2023) who recently showed that the CAMS reanalysis have low performances in  
792 estimating solar irradiance during high AOD episodes like the one studied here.  
793 Furthermore, the comparison reveals that incorporating dust in the simulation reduces  
794 surface solar irradiance by 18% in this case study. This reduction is notably higher but  
795 remains within the same order of magnitude as previous studies that integrated dust aerosol  
796 information for solar estimation. For example, Masoom et al. (2021) in India and Mostamandi  
797 et al. (2023) in the Arabian Peninsula reported GHI reductions due to dust of approximately  
798 5-10%. This discrepancy underscores the potential variability of the dust impact on solar  
799 irradiance depending on the method used to account for dust effects in the simulations. In  
800 light of the anticipated expansion of PV production in West Africa, this point underscores the  
801 potential consequences of such dust events if they are not accurately predicted.

802

803 The evaluation of local surface temperature (Fig. 4) reveals contrasting results regarding the  
804 effectiveness of the coupled approach. It demonstrates an average local MAE reduction of  
805 approximately 10% compared to the WRF-only simulation. However, the main differences  
806 occur mainly at night, when no photovoltaic is produced, as previously observed by Yue et  
807 al. (2010) and Briant et al. (2017). It can be attributed to the opposing radiative forcing

808 effects of dust aerosols across different wavelength ranges. In the case of longwave, which  
809 corresponds to terrestrial radiation, the presence of dust aerosols has a warming effect.  
810 Conversely, for shortwave, which corresponds to solar radiation, the presence of dust  
811 aerosols induces a cooling effect. Consequently, during night-time when solely terrestrial  
812 radiation is present, there is an increase in surface temperature. During day-time a  
813 competition between the warming effect of terrestrial radiation and the cooling effect of solar  
814 radiation ensues. The net impact is a decrease in surface temperature, indicating that the  
815 effect of solar radiation dominates, with the cooling effect exceeding the warming effect  
816 (Sokolik and Toon, 1999).

817 The regional evaluation in Fig. 5 confirms these contrasting results and indicates a reduction  
818 of regional MAE by about 14% with the coupling rather than WRF alone. The overestimation  
819 of surface temperature in dusty areas with the coupling, not present in the WRF only  
820 simulation, reveals the dominant aerosol warming effect during night time as compared to  
821 the cooling effect during daytime. These results align with those of Briant et al. (2017), who  
822 estimated dust-induced warming of up to +5°C during nighttime and cooling of approximately  
823 -1°C during daytime in a 2012 dust event in West Africa. These statements strongly depend  
824 on the accuracy of the ERA5 reanalysis which serves as reference. ERA5 integrates data  
825 assimilation of temperature and incorporates aerosol radiative effects through prescribed  
826 monthly climatologies from the GOCART model, but does not dynamically simulate aerosols.  
827 Due to the limited ground measurements in the Saharan region to constrain the reanalysis,  
828 and to the significant biases that can come when considering a coarse climatology for the  
829 radiative effects of aerosols to represent an intense dust event, it is possible that ERA5  
830 underestimates the aerosol effect in dusty areas.

831

832 Nevertheless, despite the improvements demonstrated in solar irradiance and surface  
833 temperature estimation, the WRF-CHIMERE simulations exhibit a notable positive bias in  
834 terms of AOD, as evidenced by the local and regional evaluations presented in Figs. 6 and  
835 7. This overestimation cannot be attributed solely to differences in aerosol concentrations, as  
836 the simulations yield markedly disparate surface concentrations of PM<sub>10</sub>, depending on the  
837 dust aerosol initial and boundary condition dataset chosen (Fig. 10), while this discrepancies  
838 do not appear in the AOD estimates. However, the results from Yahi et al. (2013) and Léon  
839 et al. (2020) emphasized the importance of considering dust plume height when linking  
840 surface PM<sub>10</sub> concentrations to AOD. Therefore, differences in the vertical distribution of the  
841 dust plume, not evaluated in this study due to the lack of quantitative observational data,  
842 could account for part of the observed discrepancies between simulated AODs and surface  
843 PM<sub>10</sub> concentrations. This excess of aerosol load may be attributed to an overestimation of  
844 emissions within the domain, but this cannot be verified as there is not any such  
845 measurement. The incoming flux of dust in the domain plays a minor role as shown in Fig.  
846 12 where the flux significantly also varies depending on the dust aerosol initial and boundary  
847 condition dataset employed, while these differences are not any more present in the  
848 simulated AOD estimates. Additionally, the underestimation of aerosol deposition, by  
849 sedimentation (not studied in this research) could be at the origin of the overestimation of the  
850 simulated dust loads. Finally, another potential explanation for these AOD biases may be the  
851 inaccuracies in the dust radiative properties incorporated in the CHIMERE model calculation  
852 (see Table S1 and S2). These depend on the mineralogical composition of the desert dust  
853 particles emitted, which are considered uniform in this work. The radiative properties of  
854 aerosols also depend on their granulometry. In the CHIMERE model, dust aerosols are  
855 treated as spherical particles in the calculation of their radiative properties using Mie theory,

856 which introduces biases. Adbiyi et al. (2023) showed that ellipsoidal dust particles have a  
857 slightly higher mass extinction efficiency compared to spherical particles. As a result,  
858 accounting for ellipsoidal dust aerosols would lead to a slight increase in AOD associated  
859 with a small decrease in GHI. This study further indicates that dust particles with radii  
860 smaller than 20.0  $\mu\text{m}$  are the primary contributors to dust AOD for shortwave radiation, with  
861 the contribution from larger particles being an order of magnitude lower. Therefore, including  
862 particles larger than 40.0  $\mu\text{m}$  in the CHIMERE model would not significantly affect AOD and  
863 GHI estimates. This is corroborated by Mostamandi et al. (2023), who demonstrated that  
864 dust particles with radii smaller than 3  $\mu\text{m}$  are primarily responsible for the reduction in solar  
865 irradiance, while particles larger than 10  $\mu\text{m}$  mainly contribute to dust deposition, which was  
866 not examined in this study.

867

868 The uncertainty associated with the choice of the large scale dust aerosol initial and  
869 boundary condition dataset is very low when considering the variables of interest for solar  
870 production, namely GHI and surface temperature (Fig. 3 and 5). This uncertainty is also low  
871 compared to the performance of simulations for AOD estimation (Fig. 7). This result is similar  
872 when examining dust emissions within the domain, which are nearly identical for the three  
873 coupled simulations (Fig. 11). This can be explained by the fact that dust emissions depend  
874 on the cube of surface wind speed (Marticorena and Bergametti, 1995) which present no  
875 significant signature of the selection of the dust aerosol initial and boundary conditions (Fig.  
876 S4). The aerosols emitted within the chosen domain are much greater than those entering,  
877 as the domain accounts for the main source zones. This is why the simulations are not that  
878 sensitive to dust aerosol large-scale dataset employed. The results regarding the uncertainty  
879 associated with the choice of the dust aerosol initial and boundary condition dataset differs  
880 when examining various elements of the dust life cycle. Indeed, aerosol size distributions  
881 vary significantly between the simulation driven with GOCART on one hand, and simulations  
882 driven with CAMS and MERRA2 on the other hand. GOCART climatology over-represents  
883 aerosols larger than 10  $\mu\text{m}$  compared to the CAMS and MERRA2 reanalyses. These  
884 differences partially account for the significant deviation in surface  $\text{PM}_{10}$  concentration  
885 estimates (Fig. 10), indicating that reanalysis-type datasets result in much higher values, up  
886 to 3 times higher, compared to climatological-type data which is closer to ground  
887 observations. The dust flux entering the domain may also partly explain these differences. In  
888 fact, this flux is very low with GOCART, with values up to 3.5 times lower than CAMS and  
889 MERRA2 (Fig. 12). The size distribution of this incoming aerosol flux is also a determining  
890 factor.

891

#### 892 **4. Conclusion and perspectives**

893 This study aims to evaluate the ability of the WRF-CHIMERE coupling to simulate GHI  
894 during a typical dust event in the dry season in West Africa. This event is characterised by a  
895 Harmattan flux associated with significant desert dust emissions over the Bodélé  
896 Depression, with the dust plume subsequently transported westward. This work  
897 demonstrates the utility of coupling a meteorological model with a desert aerosol life cycle  
898 model to represent such events, particularly for improving solar forecasts. Indeed, GHI  
899 estimations are markedly enhanced with this approach compared to using a meteorological  
900 model alone with a 75% reduction of local MAE. Nevertheless, the performance of the WRF-  
901 CHIMERE simulations in representing the aerosol load of this event is more controversial.  
902 There is an overall overestimation of AOD and  $\text{PM}_{10}$  surface concentration by the coupled  
903 model in the North Sahelian-Saharan zone.

904 This work also aims at investigating whether the performance of the simulations can be  
905 improved by changing the dust aerosol initial and boundary condition dataset, and to  
906 estimate the uncertainty associated with this choice. The results show that this selection has  
907 almost no influence on the estimation of the solar irradiance, surface temperature and AOD.  
908 On the contrary, the choice of the dust aerosol initial and boundary condition dataset has a  
909 significant impact on the surface PM<sub>10</sub> concentration and the aerosol size distribution.

910

911 This work outlines new research perspectives. Firstly, we observe the difficulty of evaluating  
912 simulations in West Africa due to the scarcity of available observations. Establishing a  
913 denser measurement network or conducting observation campaigns, particularly for GHI,  
914 would help research on solar estimation and forecasting in this region. Additionally, the  
915 WRF-CHIMERE simulations demonstrate significant biases in terms of AOD and PM<sub>10</sub>  
916 surface concentration which are not fully explained here. One potential explanation for this is  
917 an overestimation of dust emission, for which no evaluation is possible. Furthermore,  
918 studying aerosol deposition (not conducted in this work) would complement the study of the  
919 desert aerosol life cycle. On the one hand, an underestimation of deposition might be a  
920 contributing factor to the overestimation of the simulated aerosol load. On the other hand,  
921 dust deposition on solar panels affects solar production by masking the available solar  
922 irradiance (soiling effect), and this should be taken into account in forecasting systems to  
923 conduct optimised cleaning operations. Finally, the study focuses on a typical dust event  
924 during the dry season, presenting essentially aerosol-radiation interaction. It could be  
925 beneficial to test such simulation configuration for more complex cases involving cloud  
926 presence. Indeed, the interaction between aerosols and clouds have a significant impact on  
927 solar forecasting by increasing albedo, extending cloud lifespan, and promoting cloud  
928 formation through increased condensation nucleus concentration (indirect aerosol effects).

929

### 930 **Code and data availability**

931 WRF namelist configuration files, CHIMERE parameter files, Python codes exploited in this  
932 study and GOCART climatology data can be found on the following Zenodo repository:

933 <https://zenodo.org/records/10808476>

934 ERA5 data can be found on the Copernicus Climate Data Store service :

935 <https://cds.climate.copernicus.eu/cdsapp#!/home>

936 CAMS data were downloaded on the Copernicus Atmosphere Data Store service :

937 <https://ads.atmosphere.copernicus.eu/cdsapp#!/home>

938 MERRA2 data can be found on the dedicated platform from NASA :

939 <https://goldsmr5.gesdisc.eosdis.nasa.gov/data/MERRA2/>

940 Data from AMMA ground measurements stations can be accessed from the dedicated  
941 website : <https://amma-catch.osug.fr/-jeux-de-donnees->

942 INDAAF web page allows access to the data : <https://indaaf.obs-mip.fr/catalogue/>

943 AERONET data measurements and inversion products are available through the following  
944 link: <https://aeronet.gsfc.nasa.gov/>

945 The MODIS satellite observations are available on the “Level-1 and Atmosphere Archive &  
946 Distribution System Distributed Active Archive Center” platform from NASA :

947 <https://ladsweb.modaps.eosdis.nasa.gov/>

948

### 949 **Author contributions**

950 LC, SA, CL conceptualised the study. LC performed the simulations, the analysis and the  
951 editions of the figures. LC, SA, CL, GB, BM, GS, CB, RL and JT discussed the results. LC  
952 wrote the paper

953

#### 954 **Competing interest**

955 The contact author has declared that none of the authors has any competing interests.

956

#### 957 **Acknowledgment**

958 This work has been supported by the NETWAT project (ANR-22-CE03-0011) operated by  
959 the French National Research Agency. To conduct the simulations, this study has benefited  
960 from access to the IPSL-SU (SPIRIT) cluster within the IPSL Mesocentre ESPRI facility,  
961 supported by the CNRS, UPMC, Labex L-IPSL, CNES and Ecole Polytechnique. The  
962 authors want to thank the WRF and CHIMERE developers for giving free access to their  
963 model. We thank the National Aeronautics and Space Agency for the availability of the  
964 MODIS and the MERRA2 data, the European Center for Medium-Range Weather Forecasts  
965 for the availability of the CAMS and ERA5 data and the investigators and staff who maintain  
966 and provide the AERONET, the INDAAF and the AMMA-CATCH observational data. Finally,  
967 we thank the Sonabel company for their contribution.

968 During the preparation of this work the authors used DeepL Write (DeepL SE) in order to  
969 improve language and readability. After using this tool/service, the authors reviewed and  
970 edited the content as needed and take full responsibility for the content of the publication.

971

#### 972 **References**

973 Adebisi, A., Kok, J.F., Murray, B.J., Ryder, C.L., Stuu, J.-B.W., Kahn, R.A., Knippertz,  
974 P., Formenti, P., Mahowald, N.M., Pérez García-Pando, C., Klose, M., Ansmann,  
975 A., Samset, B.H., Ito, A., Balkanski, Y., Di Biagio, C., Romanias, M.N., Huang, Y.,  
976 Meng, J., 2023. A review of coarse mineral dust in the Earth system. *Aeolian*  
977 *Research* 60, 100849. <https://doi.org/10.1016/j.aeolia.2022.100849>

978 Africa Energy Outlook 2022, n.d.

979 Aidara, M.C., Fam, P.A., Danso, D.K., Mortey, E.M., Mbaye, A., Ndiaye, M.L.,  
980 Bonkaney, A.L., Adamou, R., Anquetin, S., Diedhiou, A., 2023. Contribution to the  
981 building of a weather information service for solar panel cleaning operations at  
982 Diass plant (Senegal, Western Sahel). *Open Geosciences* 15.  
983 <https://doi.org/10.1515/geo-2022-0449>

984 Alfaro, S.C., Gomes, L., 2001. Modeling mineral aerosol production by wind erosion:  
985 Emission intensities and aerosol size distributions in source areas. *Journal of*  
986 *Geophysical Research: Atmospheres* 106, 18075–18084.  
987 <https://doi.org/10.1029/2000JD900339>

988 AMMA-CATCH (2005): Meteorological dataset (including radiative budget and soil  
989 variables), within the Niamey square degree site (16 000 km<sup>2</sup>), Niger. IRD, CNRS-  
990 INSU, OSUG, OMP, OREME. [doi:10.17178/AMMA-CATCH.AL.Met\\_Nc](https://doi.org/10.17178/AMMA-CATCH.AL.Met_Nc)

991 Arakawa, A., 2004. The Cumulus Parameterization Problem: Past, Present, and Future.  
992 *Journal of Climate* 17, 2493–2525. [https://doi.org/10.1175/1520-0442\(2004\)017<2493:RATCPP>2.0.CO;2](https://doi.org/10.1175/1520-0442(2004)017<2493:RATCPP>2.0.CO;2)

993

994 Bergametti, G., Marticorena, B., Rajot, J.L., Chatenet, B., Féron, A., Gaimoz, C., Siour,  
995 G., Coulibaly, M., Koné, I., Maman, A., Zakou, A., 2017. Dust Uplift Potential in the  
996 Central Sahel: An Analysis Based on 10 years of Meteorological Measurements at  
997 High Temporal Resolution. *Journal of Geophysical Research: Atmospheres* 122,  
998 12,433-12,448. <https://doi.org/10.1002/2017JD027471>

999 Bian, H., Prather, M.J., n.d. Fast-J2: Accurate Simulation of Stratospheric Photolysis in  
1000 Global Chemical Models.

1001 Bou Karam, D., Flamant, C., Tulet, P., Chaboureau, J.-P., Dabas, A., Todd, M.C., 2009.  
1002 Estimate of Sahelian dust emissions in the intertropical discontinuity region of the  
1003 West African Monsoon. *Journal of Geophysical Research: Atmospheres* 114.  
1004 <https://doi.org/10.1029/2008JD011444>

1005 Briant, R., Tuccella, P., Deroubaix, A., Khvorostyanov, D., Menut, L., Mailler, S.,  
1006 Turquety, S., 2017. Aerosol–radiation interaction modelling using online coupling  
1007 between the WRF 3.7.1 meteorological model and the CHIMERE 2016 chemistry-  
1008 transport model, through the OASIS3-MCT coupler. *Geoscientific Model*  
1009 *Development* 10, 927–944. <https://doi.org/10.5194/gmd-10-927-2017>

1010 Clauzel, L., Anquetin, S., Lavaysse, C., Tremoy, G., Raynaud, D., 2024. West African  
1011 operational daily solar forecast errors and their link with meteorological conditions.  
1012 *Renewable Energy* 224, 120101. <https://doi.org/10.1016/j.renene.2024.120101>

1013 d’Almeida, G.A., 1986. A Model for Saharan Dust Transport. *Journal of Applied*  
1014 *Meteorology and Climatology* 25, 903–916. [https://doi.org/10.1175/1520-0450\(1986\)025<0903:AMFSDT>2.0.CO;2](https://doi.org/10.1175/1520-0450(1986)025<0903:AMFSDT>2.0.CO;2)

1015 Dajuma, A., Yahaya, S., Touré, S., Diedhiou, A., Adamou, R., Konaré, A., Sido, M.,  
1016 Golba, M., 2016. Sensitivity of Solar Photovoltaic Panel Efficiency to Weather and  
1017 Dust over West Africa: Comparative Experimental Study between Niamey (Niger)  
1018 and Abidjan (Côte d’Ivoire). *Computational Water, Energy, and Environmental*  
1019 *Engineering* 5, 123–147. <https://doi.org/10.4236/cweee.2016.54012>

1020 Diabaté, L., Blanc, P., Wald, L., 2004. Solar radiation climate in Africa. *Solar Energy* 76,  
1021 733–744.

1022 Diop, D., Drame, M.S., Diallo, M., Malec, D., Mary, D., Guillot, P., 2020. Modelling of  
1023 Photovoltaic Modules Optical Losses Due to Saharan Dust Deposition in Dakar,  
1024 Senegal, West Africa. *Smart Grid and Renewable Energy* 11, 89.  
1025 <https://doi.org/10.4236/sgre.2020.117007>

1026 Dubovik, O., King, M.D., 2000. A flexible inversion algorithm for retrieval of aerosol  
1027 optical properties from Sun and sky radiance measurements. *Journal of*  
1028 *Geophysical Research: Atmospheres* 105, 20673–20696.  
1029 <https://doi.org/10.1029/2000JD900282>

1030 Engelstaedter, S., Tegen, I., Washington, R., 2006. North African dust emissions and  
1031 transport. *Earth-Science Reviews* 79, 73–100.  
1032 <https://doi.org/10.1016/j.earscirev.2006.06.004>

1033



1034 Engelstaedter, S., Washington, R., 2007. Atmospheric controls on the annual cycle of  
1035 North African dust. *Journal of Geophysical Research: Atmospheres* 112.  
1036 <https://doi.org/10.1029/2006JD007195>

1037 Evans, M., Knippertz, P., Akpo, A., Allan, R.P., Amekudzi, L., Brooks, B., Chiu, J.C.,  
1038 Coe, H., Fink, A.H., Flamant, C., Jegede, O.O., Leal-Liousse, C., Lohou, F.,  
1039 Kalthoff, N., Mari, C., Marsham, J.H., Yoboué, V., Zumsprekel, C.R., 2018. Policy  
1040 findings from the DACCIWA Project. Zenodo.  
1041 <https://doi.org/10.5281/ZENODO.1476843>

1042 El Alani, O., Ghennioui, A., Ghennioui, H., Saint-Drenan, Y.-M., Blanc, P., 2020.  
1043 Evaluation of 24-hours forecasts of global solar irradiation from IFS, GFS and  
1044 McClear models.

1045 Fécan, F., Marticorena, B., Bergametti, G., 1998. Parametrization of the increase of the  
1046 aeolian erosion threshold wind friction velocity due to soil moisture for arid and  
1047 semi-arid areas. *Annales Geophysicae* 17, 149–157.  
1048 <https://doi.org/10.1007/s00585-999-0149-7>

1049 Flamant, C., Chaboureau, J.-P., Delanoë, J., Gaetani, M., Jamet, C., Lavaysse, C.,  
1050 Bock, O., Borne, M., Cazenave, Q., Coutris, P., Cuesta, J., Menut, L., Aubry, C.,  
1051 Benedetti, A., Bosser, P., Bounissou, S., Caudoux, C., Collomb, H., Donal, T.,  
1052 Febvre, G., Fehr, T., Fink, A.H., Formenti, P., Araujo, N.G., Knippertz, P., Lecuyer,  
1053 E., Andrade, M.N., Langué, C.G.N., Jonville, T., Schwarzenboeck, A., Takeishi, A.,  
1054 2024. Cyclogenesis in the Tropical Atlantic: First Scientific Highlights from the  
1055 Clouds–Atmospheric Dynamics–Dust Interactions in West Africa (CADDIWA) Field  
1056 Campaign. *Bulletin of the American Meteorological Society* 105, E387–E417.  
1057 <https://doi.org/10.1175/BAMS-D-23-0230.1>

1058 Gelaro, R., McCarty, W., Suárez, M.J., Todling, R., Molod, A., Takacs, L., Randles,  
1059 C.A., Darmenov, A., Bosilovich, M.G., Reichle, R., Wargan, K., Coy, L., Cullather,  
1060 R., Draper, C., Akella, S., Buchard, V., Conaty, A., Silva, A.M. da, Gu, W., Kim, G.-  
1061 K., Koster, R., Lucchesi, R., Merkova, D., Nielsen, J.E., Partyka, G., Pawson, S.,  
1062 Putman, W., Rienecker, M., Schubert, S.D., Sienkiewicz, M., Zhao, B., 2017. The  
1063 Modern-Era Retrospective Analysis for Research and Applications, Version 2  
1064 (MERRA-2). *Journal of Climate* 30, 5419–5454. <https://doi.org/10.1175/JCLI-D-16-0758.1>

1066 Giles, D.M., Sinyuk, A., Sorokin, M.G., Schafer, J.S., Smirnov, A., Slutsker, I., Eck, T.F.,  
1067 Holben, B.N., Lewis, J.R., Campbell, J.R., Welton, E.J., Korkin, S.V., Lyapustin,  
1068 A.I., 2019. Advancements in the Aerosol Robotic Network (AERONET) Version 3  
1069 database – automated near-real-time quality control algorithm with improved cloud  
1070 screening for Sun photometer aerosol optical depth (AOD) measurements.  
1071 *Atmospheric Measurement Techniques* 12, 169–209. <https://doi.org/10.5194/amt-12-169-2019>

1073 Ginoux, P., Chin, M., Tegen, I., Prospero, J.M., Holben, B., Dubovik, O., Lin, S.-J.,  
1074 2001. Sources and distributions of dust aerosols simulated with the GOCART

1075 model. *Journal of Geophysical Research: Atmospheres* 106, 20255–20273.  
1076 <https://doi.org/10.1029/2000JD000053>

1077 Hauglustaine, D.A., Hourdin, F., Jourdain, L., Filiberti, M.-A., Walters, S., Lamarque, J.-  
1078 F., Holland, E.A., 2004. Interactive chemistry in the Laboratoire de Météorologie  
1079 Dynamique general circulation model: Description and background tropospheric  
1080 chemistry evaluation. *Journal of Geophysical Research: Atmospheres* 109.  
1081 <https://doi.org/10.1029/2003JD003957>

1082 Hersbach, H., Bell, B., Berrisford, P., Hirahara, S., Horányi, A., Muñoz-Sabater, J.,  
1083 Nicolas, J., Peubey, C., Radu, R., Schepers, D., Simmons, A., Soci, C., Abdalla, S.,  
1084 Abellan, X., Balsamo, G., Bechtold, P., Biavati, G., Bidlot, J., Bonavita, M., De  
1085 Chiara, G., Dahlgren, P., Dee, D., Diamantakis, M., Dragani, R., Flemming, J.,  
1086 Forbes, R., Fuentes, M., Geer, A., Haimberger, L., Healy, S., Hogan, R.J., Hólm,  
1087 E., Janisková, M., Keeley, S., Laloyaux, P., Lopez, P., Lupu, C., Radnoti, G., de  
1088 Rosnay, P., Rozum, I., Vamborg, F., Villaume, S., Thépaut, J.-N., 2020. The ERA5  
1089 global reanalysis. *Quarterly Journal of the Royal Meteorological Society* 146, 1999–  
1090 2049. <https://doi.org/10.1002/qj.3803>

1091 Holben, B.N., Eck, T.F., Slutsker, I., Tanré, D., Buis, J.P., Setzer, A., Vermote, E.,  
1092 Reagan, J.A., Kaufman, Y.J., Nakajima, T., Lavenu, F., Jankowiak, I., Smirnov, A.,  
1093 1998. AERONET—A Federated Instrument Network and Data Archive for Aerosol  
1094 Characterization. *Remote Sensing of Environment* 66, 1–16.  
1095 [https://doi.org/10.1016/S0034-4257\(98\)00031-5](https://doi.org/10.1016/S0034-4257(98)00031-5)

1096 Hu, X.-M., Klein, P.M., Xue, M., 2013. Evaluation of the updated YSU planetary  
1097 boundary layer scheme within WRF for wind resource and air quality assessments.  
1098 *Journal of Geophysical Research: Atmospheres* 118, 10,490-10,505.  
1099 <https://doi.org/10.1002/jgrd.50823>

1100 Iacono, M.J., Delamere, J.S., Mlawer, E.J., Shephard, M.W., Clough, S.A., Collins,  
1101 W.D., 2008. Radiative forcing by long-lived greenhouse gases: Calculations with  
1102 the AER radiative transfer models. *Journal of Geophysical Research: Atmospheres*  
1103 113. <https://doi.org/10.1029/2008JD009944>

1104 Inness, A., Ades, M., Agustí-Panareda, A., Barré, J., Benedictow, A., Blechschmidt, A.-  
1105 M., Dominguez, J.J., Engelen, R., Eskes, H., Flemming, J., Huijnen, V., Jones, L.,  
1106 Kipling, Z., Massart, S., Parrington, M., Peuch, V.-H., Razinger, M., Remy, S.,  
1107 Schulz, M., Suttie, M., 2019. The CAMS reanalysis of atmospheric composition.  
1108 *Atmos. Chem. Phys.* 19, 3515–3556. <https://doi.org/10.5194/acp-19-3515-2019>

1109 Jiménez, P.A., Dudhia, J., González-Rouco, J.F., Navarro, J., Montávez, J.P., García-  
1110 Bustamante, E., 2012. A Revised Scheme for the WRF Surface Layer Formulation.  
1111 *Monthly Weather Review* 140, 898–918. [https://doi.org/10.1175/MWR-D-11-  
1112 00056.1](https://doi.org/10.1175/MWR-D-11-00056.1)

1113 Jimenez, P.A., Hacker, J.P., Dudhia, J., Haupt, S.E., Ruiz-Arias, J.A., Gueymard, C.A.,  
1114 Thompson, G., Eidhammer, T., Deng, A., 2016. WRF-Solar: Description and Clear-  
1115 Sky Assessment of an Augmented NWP Model for Solar Power Prediction. *Bulletin*

1116 of the American Meteorological Society 97, 1249–1264.  
1117 <https://doi.org/10.1175/BAMS-D-14-00279.1>

1118 Kaly, F., Marticorena, B., Chatenet, B., Rajot, J.L., Janicot, S., Niang, A., Yah, H.,  
1119 Thiria, S., Maman, A., Zakou, A., Coulibaly, B.S., Coulibaly, M., Koné, I., Traoré, S.,  
1120 Diallo, A., Ndiaye, T., 2015. Variability of mineral dust concentrations over West  
1121 Africa monitored by the Sahelian Dust Transect. *Atmos. Res.* 164–165, 226–241.  
1122 <https://doi.org/10.1016/j.atmosres.2015.05.011>

1123 Kandler, K., Benker, N., Bundke, U., Cuevas, E., Ebert, M., Knippertz, P., Rodríguez, S.,  
1124 Schütz, L., Weinbruch, S., 2007. Chemical composition and complex refractive  
1125 index of Saharan Mineral Dust at Izaña, Tenerife (Spain) derived by electron  
1126 microscopy. *Atmospheric Environment* 41, 8058–8074.  
1127 <https://doi.org/10.1016/j.atmosenv.2007.06.047>

1128 Klose, M., Shao, Y., Karremann, M.K., Fink, A.H., 2010. Sahel dust zone and synoptic  
1129 background. *Geophysical Research Letters* 37.  
1130 <https://doi.org/10.1029/2010GL042816>

1131 Klüser, L., Killius, N., Gesell, G., 2015. APOLLO\_NG &ndash; a probabilistic  
1132 interpretation of the APOLLO legacy for AVHRR heritage channels. *Atmospheric*  
1133 *Measurement Techniques* 8, 4155–4170. <https://doi.org/10.5194/amt-8-4155-2015>

1134 Kok, J.F., Adebisi, A.A., Albani, S., Balkanski, Y., Checa-Garcia, R., Chin, M., Colarco,  
1135 P.R., Hamilton, D.S., Huang, Y., Ito, A., Klose, M., Li, L., Mahowald, N.M., Miller,  
1136 R.L., Obiso, V., Pérez García-Pando, C., Rocha-Lima, A., Wan, J.S., 2021.  
1137 Contribution of the world's main dust source regions to the global cycle of desert  
1138 dust. *Atmos. Chem. Phys.* 21, 8169–8193. [https://doi.org/10.5194/acp-21-8169-](https://doi.org/10.5194/acp-21-8169-2021)  
1139 [2021](https://doi.org/10.5194/acp-21-8169-2021)

1140 Lefèvre M., 2022, CAMS solar radiation evaluation and quality assurance report #34,  
1141 March-May 2021, ECMWF COPERNICUS REPORT,  
1142 [https://atmosphere.copernicus.eu/sites/default/files/custom-uploads/EQC-solar/](https://atmosphere.copernicus.eu/sites/default/files/custom-uploads/EQC-solar/CAMS2_73_2021SC1_D1.3.1-2021Q4_RAD_validation_report_MAM2021_v1.pdf)  
1143 [CAMS2\\_73\\_2021SC1\\_D1.3.1-2021Q4\\_RAD\\_validation\\_report\\_MAM2021\\_v1.pdf](https://atmosphere.copernicus.eu/sites/default/files/custom-uploads/EQC-solar/CAMS2_73_2021SC1_D1.3.1-2021Q4_RAD_validation_report_MAM2021_v1.pdf)

1144 Legates, D.R., McCabe, G.J., 2013. A refined index of model performance: a rejoinder.  
1145 *International Journal of Climatology* 33, 1053–1056.  
1146 <https://doi.org/10.1002/joc.3487>

1147 Léon, J.-F., Martiny, N., Merlet, S., 2020. A Multi Linear Regression Model to Derive  
1148 Dust PM10 in the Sahel Using AERONET Aerosol Optical Depth and CALIOP  
1149 Aerosol Layer Products. *Remote Sensing* 12, 3099.  
1150 <https://doi.org/10.3390/rs12183099>

1151 Marham, J.H., Parker, D.J., Grams, C.M., Grey, W.M.F., Johnson, B.T., 2008.  
1152 Observations of mesoscale and boundary-layer circulations affecting dust uplift and  
1153 transport in the Saharan boundary layer (preprint). [https://doi.org/10.5194/acpd-8-](https://doi.org/10.5194/acpd-8-8817-2008)  
1154 [8817-2008](https://doi.org/10.5194/acpd-8-8817-2008)

1155 Marticorena, B., Bergametti, G., 1995. Modeling the atmospheric dust cycle: 1. Design  
1156 of a soil-derived dust emission scheme. *Journal of Geophysical Research:*  
1157 *Atmospheres* 100, 16415–16430. <https://doi.org/10.1029/95JD00690>  
1158 Marticorena, B., Chatenet, B., Rajot, J.L., Traoré, S., Coulibaly, M., Diallo, A., Koné, I.,  
1159 Maman, A., NDiaye, T., Zakou, A., 2010. Temporal variability of mineral dust  
1160 concentrations over West Africa: analyses of a pluriannual monitoring from the  
1161 AMMA Sahelian Dust Transect. *Atmos. Chem. Phys.* 10, 8899–8915.  
1162 <https://doi.org/10.5194/acp-10-8899-2010>  
1163 Marticorena, B., Dorego, G.S., Rajot, J.L., Bouet, C., Allègre, M., Chatenet, B., Féron,  
1164 A., Gaimoz, C., Siour, G., Valorso, R., Diop, M., Der Ba, S., Rokhy N'Diaye, G.,  
1165 Séné, M. & Thiam, A. (2021). Air temperature, Bambey, Senegal. [dataset]. Aeris.  
1166 <https://doi.org/10.25326/263>  
1167 Marticorena, B., Dorego, G.S., Rajot, J.L., Bouet, C., Allègre, M., Chatenet, B., Féron,  
1168 A., Gaimoz, C., Maisonneuve, F., Siour, G., Valorso, R., Diop, M., Der Ba, S.,  
1169 Rokhy N'Diaye, G., Séné, M. & Thiam, A. (2021). PM10 concentration, Bambey,  
1170 Senegal. [dataset]. Aeris. <https://doi.org/10.25326/267>  
1171 Masoom, A., 2021. Forecasting dust impact on solar energy using remote sensing and  
1172 modeling techniques. *Solar Energy* 16.  
1173 Mazzeo, A., Burrow, M., Quinn, A., Marais, E.A., Singh, A., Ng'ang'a, D., Gatari, M.J.,  
1174 Pope, F.D., 2022. Evaluation of the WRF and CHIMERE models for the simulation  
1175 of PM<sub>2.5</sub> in large East African urban conurbations. *Atmospheric Chemistry and*  
1176 *Physics* 22, 10677–10701. <https://doi.org/10.5194/acp-22-10677-2022>  
1177 Menut, L., 2023. Variability and combination as an ensemble of mineral dust forecasts  
1178 during the 2021 CADDIWA experiment using the WRF 3.7.1 and CHIMERE  
1179 v2020r3 models. *Geoscientific Model Development* 16, 4265–4281.  
1180 <https://doi.org/10.5194/gmd-16-4265-2023>  
1181 Menut, L., Bessagnet, B., Briant, R., Cholakian, A., Couvidat, F., Mailler, S., Pennel, R.,  
1182 Siour, G., Tuccella, P., Turquety, S., Valari, M., 2021. The CHIMERE v2020r1  
1183 online chemistry-transport model. *Geoscientific Model Development* 14, 6781–  
1184 6811. <https://doi.org/10.5194/gmd-14-6781-2021>  
1185 Menut, L., Siour, G., Mailler, S., Couvidat, F., Bessagnet, B., 2016. Observations and  
1186 regional modeling of aerosol optical properties, speciation and size distribution over  
1187 Northern Africa and western Europe. *Atmos. Chem. Phys.* 16, 12961–12982.  
1188 <https://doi.org/10.5194/acp-16-12961-2016>  
1189 MODIS Atmosphere Science Team, 2017. MODIS/Terra Aerosol Cloud Water Vapor  
1190 Ozone Daily L3 Global 1Deg CMG. [https://doi.org/10.5067/MODIS/MOD08\\_D3.061](https://doi.org/10.5067/MODIS/MOD08_D3.061)  
1191 Mostamandi, S., Ukhov, A., Engelbrecht, J., Shevchenko, I., Osipov, S., Stenchikov, G.,  
1192 2023. Fine and Coarse Dust Effects on Radiative Forcing, Mass Deposition, and  
1193 Solar Devices Over the Middle East. *Journal of Geophysical Research:*  
1194 *Atmospheres* 128, e2023JD039479. <https://doi.org/10.1029/2023JD039479>

1195 Mueller, R., Pfeifroth, U., Traeger-Chatterjee, C., 2015. Towards Optimal Aerosol  
1196 Information for the Retrieval of Solar Surface Radiation Using Heliosat. *Atmosphere*  
1197 6, 863–878. <https://doi.org/10.3390/atmos6070863>

1198 Niu, G.-Y., Yang, Z.-L., Mitchell, K.E., Chen, F., Ek, M.B., Barlage, M., Kumar, A.,  
1199 Manning, K., Niyogi, D., Rosero, E., Tewari, M., Xia, Y., 2011. The community  
1200 Noah land surface model with multiparameterization options (Noah-MP): 1. Model  
1201 description and evaluation with local-scale measurements. *Journal of Geophysical*  
1202 *Research: Atmospheres* 116. <https://doi.org/10.1029/2010JD015139>

1203 Ochiegbu, D.C., 2021. Event of harmattan dust transport in Kano State of Nigeria.  
1204 *IJSRP* 11, 205–210. <https://doi.org/10.29322/IJSRP.11.08.2021.p11628>

1205 Plain, N., Hingray, B., Mathy, S., 2019. Accounting for low solar resource days to size  
1206 100% solar microgrids power systems in Africa. *Renewable Energy* 131, 448–458.  
1207 <https://doi.org/10.1016/j.renene.2018.07.036>

1208 Prigent, C., Jiménez, C., Catherinot, J., 2012. Comparison of satellite microwave  
1209 backscattering (ASCAT) and visible/near-infrared reflectances (PARASOL) for the  
1210 estimation of aeolian aerodynamic roughness length in arid and semi-arid regions.  
1211 *Atmospheric Measurement Techniques* 5, 2703–2712. [https://doi.org/10.5194/amt-](https://doi.org/10.5194/amt-5-2703-2012)  
1212 [5-2703-2012](https://doi.org/10.5194/amt-5-2703-2012)

1213 Prospero, J.M., Ginoux, P., Torres, O., Nicholson, S.E., Gill, T.E., 2002. Environmental  
1214 Characterization of Global Sources of Atmospheric Soil Dust Identified with the  
1215 Nimbus 7 Total Ozone Mapping Spectrometer (toms) Absorbing Aerosol Product.  
1216 *Reviews of Geophysics* 40, 2-1-2–31. <https://doi.org/10.1029/2000RG000095>

1217 Qu, Z., Oumbe, A., Blanc, P., Espinar, B., Gesell, G., Gschwind, B., Klüser, L., Lefèvre,  
1218 M., Saboret, L., Schroedter-Homscheidt, M., Wald, L., 2017. Fast radiative transfer  
1219 parameterisation for assessing the surface solar irradiance: The Heliosat-4 method.  
1220 *Meteorologische Zeitschrift* 33–57. <https://doi.org/10.1127/metz/2016/0781>

1221 Rajot, J.L., Abdourhamane Touré, A., Marticorena, B., Bouet, C., Allègre, M., Chatenet,  
1222 B., Féron, A., Gaimoz, C., Siour, G., Valorso, R., Maman, A. & Zakou, A. (2010). Air  
1223 temperature, Banizoumbou, Niger. [dataset]. AERIS. <https://doi.org/10.25326/210>

1224 Rajot, J.L., Boubacar, A., Marticorena, B., Bouet, C., Allègre, M., Chatenet, B., Féron,  
1225 A., Gaimoz, C., Siour, G., Valorso, R., Coulibaly, S.B., Kouyaté, Z., Coulibaly, B.,  
1226 Coulibaly, M., Koné, I. & Traoré, S. (2010). Air temperature, Cinzana, Mali.  
1227 [dataset]. AERIS. <https://doi.org/10.25326/269>

1228 Rajot, J.L., Boubacar, A., Marticorena, B., Bouet, C., Allègre, M., Chatenet, B., Féron,  
1229 A., Gaimoz, C., Maisonneuve, F., Siour, G., Valorso, R., Coulibaly, S.B., Kouyaté,  
1230 Z., Coulibaly, B., Coulibaly, M., Koné, I. & Traoré, S. (2010). PM10 concentration,  
1231 Cinzana, Mali. [dataset]. AERIS. <https://doi.org/10.25326/268>

1232 Redelsperger, J.-L., Diedhiou, A., Flamant, C., Janicot, S., Lafore, J.-P., Lebel, T.,  
1233 Polcher, J., Bourlès, B., Caniaux, G., Rosnay, P. de, Desbois, M., Eymard, L.,  
1234 Fontaine, B., Geneau, I., Ginoux, K., Hoepffner, M., Kane, C.S.E., Law, K.S., Mari,  
1235 C., Marticorena, B., Mougin, É., Pelon, J., Peugeot, C., Protat, A., Roux, F., Sultan,

1236 B., Akker, E. van den, 2006. Amma, une étude multidisciplinaire de la mousson  
1237 ouest-africaine. *La Météorologie* 54, 22. <https://doi.org/10.4267/2042/20098>

1238 Sawadogo, W., Bliedernicht, J., Fersch, B., Salack, S., Guug, S., Diallo, B., Ogunjobi,  
1239 Kehinde.O., Nakoulma, G., Tanu, M., Meilinger, S., Kunstmann, H., 2023. Hourly  
1240 global horizontal irradiance over West Africa: A case study of one-year satellite-  
1241 and reanalysis-derived estimates vs. in situ measurements. *Renewable Energy*  
1242 216, 119066. <https://doi.org/10.1016/j.renene.2023.119066>

1243 Sawadogo, W., Fersch, B., Bliedernicht, J., Meilinger, S., Rummler, T., Salack, S., Guug,  
1244 S., Kunstmann, H., 2024. Evaluation of the WRF-solar model for 72-hour ahead  
1245 forecasts of global horizontal irradiance in West Africa: A case study for Ghana.  
1246 *Solar Energy* 271, 112413. <https://doi.org/10.1016/j.solener.2024.112413>

1247 Schepanski, K., Tegen, I., Todd, M.C., Heinold, B., Bönisch, G., Laurent, B., Macke, A.,  
1248 2009. Meteorological processes forcing Saharan dust emission inferred from MSG-  
1249 SEVIRI observations of subdaily dust source activation and numerical models.  
1250 *Journal of Geophysical Research: Atmospheres* 114.  
1251 <https://doi.org/10.1029/2008JD010325>

1252 Schroedter-Homscheidt, M., Azam, F., Betcke, J., Hanrieder, N., Lefevre, M., Saboret,  
1253 L., Saint-Drenan, Y.-M., 2022. Surface solar irradiation retrieval from MSG/SEVIRI  
1254 based on APOLLO Next Generation and HELIOSAT-4 methods. *Meteorologische*  
1255 *Zeitschrift* 31, 455–476.

1256 Shao, Y., Lu, H., 2000. A simple expression for wind erosion threshold friction velocity.  
1257 *Journal of Geophysical Research: Atmospheres* 105, 22437–22443.  
1258 <https://doi.org/10.1029/2000JD900304>

1259 Skamarock, W.C., Klemp, J.B., Dudhia, J., Gill, D.O., Barker, D.M., Duda, M.G., Huang,  
1260 X.-Y., Wang, W., Powers, J.G., n.d. A Description of the Advanced Research WRF  
1261 Version 3.

1262 Sokolik, I.N., Toon, O.B., 1999. Incorporation of mineralogical composition into models  
1263 of the radiative properties of mineral aerosol from UV to IR wavelengths. *J.*  
1264 *Geophys. Res.* 104, 9423–9444. <https://doi.org/10.1029/1998JD200048>

1265 The Paris Agreement | UNFCCC [WWW Document], n.d. URL  
1266 <https://unfccc.int/process-and-meetings/the-paris-agreement> (accessed 2.12.24).

1267 Thompson, G., Eidhammer, T., 2014. A Study of Aerosol Impacts on Clouds and  
1268 Precipitation Development in a Large Winter Cyclone. *Journal of the Atmospheric*  
1269 *Sciences* 71, 3636–3658. <https://doi.org/10.1175/JAS-D-13-0305.1>

1270 Tuccella, P., Menut, L., Briant, R., Deroubaix, A., Khvorostyanov, D., Mailler, S., Siour,  
1271 G., Turquety, S., 2019. Implementation of Aerosol-Cloud Interaction within WRF-  
1272 CHIMERE Online Coupled Model: Evaluation and Investigation of the Indirect  
1273 Radiative Effect from Anthropogenic Emission Reduction on the Benelux Union.  
1274 *Atmosphere* 10, 20. <https://doi.org/10.3390/atmos10010020>

1275 Vautard, R., Bessagnet, B., Chin, M., Menut, L., 2005. On the contribution of natural  
1276 Aeolian sources to particulate matter concentrations in Europe: Testing hypotheses

1277 with a modelling approach. *Atmospheric Environment* 39, 3291–3303.  
1278 <https://doi.org/10.1016/j.atmosenv.2005.01.051>

1279 Washington, R., Todd, M.C., 2005. Atmospheric controls on mineral dust emission from  
1280 the Bodélé Depression, Chad: The role of the low level jet. *Geophysical Research*  
1281 *Letters* 32. <https://doi.org/10.1029/2005GL023597>

1282 Washington, R., Todd, M.C., Lizcano, G., Tegen, I., Flamant, C., Koren, I., Ginoux, P.,  
1283 Engelstaedter, S., Bristow, C.S., Zender, C.S., Goudie, A.S., Warren, A., Prospero,  
1284 J.M., 2006. Links between topography, wind, deflation, lakes and dust: The case of  
1285 the Bodélé Depression, Chad. *Geophysical Research Letters* 33.  
1286 <https://doi.org/10.1029/2006GL025827>

1287 Wild, O., Zhu, X., Prather, M.J., n.d. Fast-J: Accurate Simulation of In- and Below-Cloud  
1288 Photolysis in Tropospheric Chemical Models.

1289 Willis, P.T., Tattelman, P., 1989. Drop-Size Distributions Associated with Intense  
1290 Rainfall. *Journal of Applied Meteorology* (1988-2005) 28, 3–15.

1291 Yahi, H., Marticorena, B., Thiria, S., Chatenet, B., Schmechtig, C., Rajot, J.L., Crepon,  
1292 M., 2013. Statistical relationship between surface PM10 concentration and aerosol  
1293 optical depth over the Sahel as a function of weather type, using neural network  
1294 methodology. *Journal of Geophysical Research: Atmospheres* 118, 13,265-13,281.  
1295 <https://doi.org/10.1002/2013JD019465>

1296 Yang, D., Bright, J.M., 2020. Worldwide validation of 8 satellite-derived and reanalysis  
1297 solar radiation products: A preliminary evaluation and overall metrics for hourly data  
1298 over 27 years. *Solar Energy, Special Issue on Grid Integration* 210, 3–19.  
1299 <https://doi.org/10.1016/j.solener.2020.04.016>

1300 Yue, X., Wang, H., Liao, H., Fan, K., 2010. Simulation of dust aerosol radiative feedback  
1301 using the GMOD: 2. Dust-climate interactions. *Journal of Geophysical Research:*  
1302 *Atmospheres* 115. <https://doi.org/10.1029/2009JD012063>

1303 Yushchenko, A., De Bono, A., Chatenoux, B., Kumar Patel, M., Ray, N., 2018. GIS-  
1304 based assessment of photovoltaic (PV) and concentrated solar power (CSP)  
1305 generation potential in West Africa. *Renewable and Sustainable Energy Reviews*  
1306 81, 2088–2103. <https://doi.org/10.1016/j.rser.2017.06.021>

1307 Zhang, L., Gong, S., Padro, J., Barrie, L., 2001. A size-segregated particle dry  
1308 deposition scheme for an atmospheric aerosol module. *Atmospheric Environment*  
1309 35, 549–560. [https://doi.org/10.1016/S1352-2310\(00\)00326-5](https://doi.org/10.1016/S1352-2310(00)00326-5)

1310 Ziane, A., Necaibia, A., Sahouane, N., Dabou, R., Mostefaoui, M., Bouraiou, A., Khelifi,  
1311 S., Rouabhia, A., Blal, M., 2021. Photovoltaic output power performance  
1312 assessment and forecasting: Impact of meteorological variables. *Solar Energy* 220,  
1313 745–757. <https://doi.org/10.1016/j.solener.2021.04.004>